www.acsnano.org

An Implant-Free Nanosystem Enabling Synergistic Oxidative Damage Mitigation and Deep Brain Stimulation for Alleviating Parkinsonian Symptoms

Chen Zhou,[†] Feifei Wu,[†] Liqing He, Huijie Yan, Zhaowei Zhang, Shuang Zhao, Wenyi Huang, Yuhao Luo, Wei Zhao, Bulong Gao, Zherui Zhang, Yaofeng Zhou, Baiheng Wu,* Junqiu Liu,* and Dingcheng Zhu*



Downloaded via HANGZHOU NORMAL UNIV on November 11, 2025 at 02:28:55 (UTC). See https://pubs.acs.org/sharingguidelines for options on how to legitimately share published articles.

Cite This: ACS Nano 2025, 19, 26715-26734



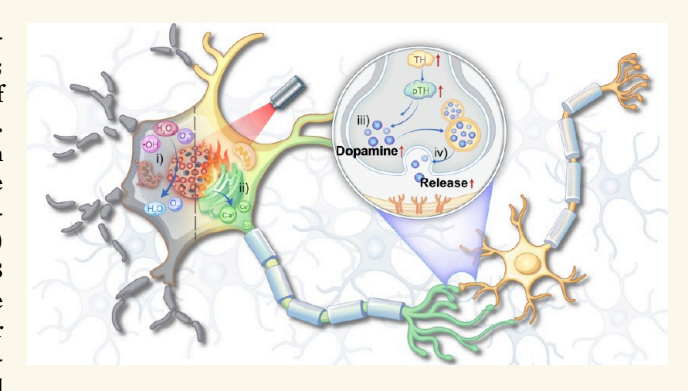
ACCESS

III Metrics & More

Article Recommendations

Supporting Information

ABSTRACT: Deep brain stimulation (DBS) effectively alleviates motor symptoms in Parkinson's disease (PD) patients; however, it necessitates permanent invasive implantation of conduits, and its therapeutic effects diminish as PD progresses. Herein, an implant-free NIR-II laser-activated intervention nanosystem that combines wireless DBS with antioxidative neuroprotection is developed to overcome the above challenges. Enzyme-like 2-(phenylselanyl)ethan-1-amine (SePh) and manganese dioxide (MnO₂) and NIR-II absorber IR-1048 (IR) are integrated onto the mesoporous polydopamine (mPDA) core to form mPDA-SeMn-IR. Upon NIR-II laser irradiation, intraventricularly injected mPDA-SeMn-IR nanoparticles effectively activate endogenously expressed inositol



1,4,5-trisphosphate receptors, leading to Ca²⁺ outflux from the endoplasmic reticulum. Ca²⁺ signaling enhances tyrosine hydroxylase expression and activity and triggers dopamine release to enhance dopaminergic function. Meanwhile, mPDA-SeMn-IR rapidly eliminates excessive reactive oxygen species, synergistically enhancing long-term DBS efficiency by increasing neuron survival and restoring neuronal function for improved dopamine secretion. *In vivo*, mPDA-SeMn-IR regulates midbrain neurons and coiling behaviors in zebrafish and considerably alleviates motor symptoms in the PD model, proposing a promising therapeutic strategy to address existing challenges in PD therapies.

KEYWORDS: deep brain stimulation, implant-free, photothermal activation, Ca^{2+} signaling, cascade nanozyme, oxidative stress mitigation

INTRODUCTION

Parkinson's disease (PD) arises from dopaminergic neuron degeneration, which disrupts dopamine biosynthesis/release and causes striatal dopamine deficiency. Dopamine replacement therapy (e.g., levodopa and dopamine agonists), the standard symptomatic treatment for PD motor dysfunction, aims to compensate for dopamine loss but exhibits short-term efficacy, medication-related complications, and dopamine dysregulation syndrome. Subthalamic nucleus deep brain stimulation (STN-DBS) is approved by the FDA for late-stage PD patients who are resistant to or experience severe side effects from dopaminergic medications. It electrically stimulates voltage-gated Ca²⁺ channels (VGCC) on residual dopaminergic neurons and augments their dopamine release (and possibly dopamine biosynthesis 4,5), thereby improving

the pathological network activity.^{5–8} However, STN-DBS necessitates the bilateral implantation of chronic electrodes deep in the STN region. Although several recent clinical trials have confirmed its effectiveness in improving motor symptoms, ^{9–11} the inherent invasiveness and associated risks, including infection and hemorrhage, dramatically limit patient acceptance.¹²

Received: April 14, 2025 Revised: July 3, 2025 Accepted: July 7, 2025 Published: July 15, 2025





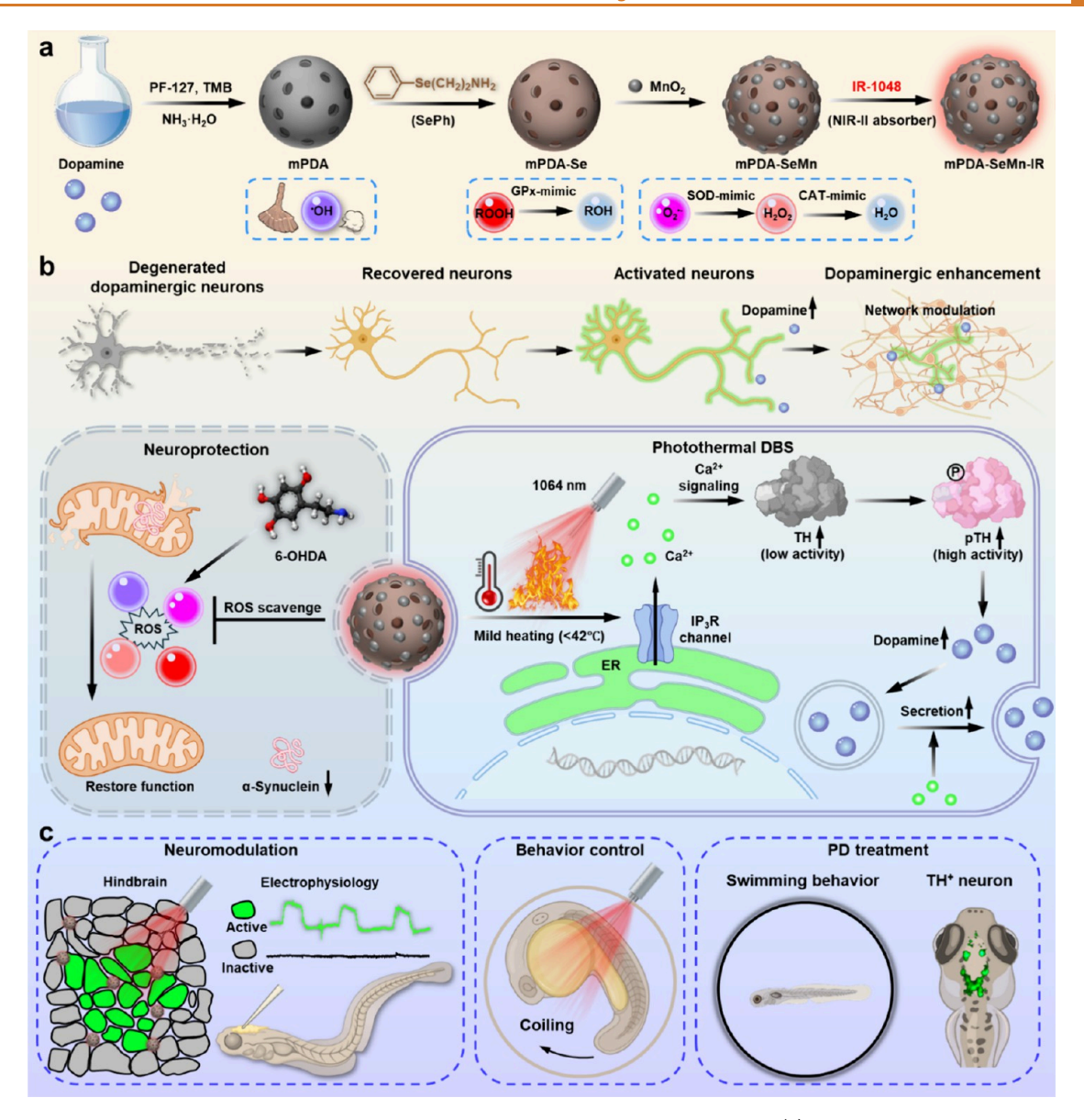


Figure 1. Schematic illustration of an implant-free multifunctional nanosystem for PD therapy. (a) The mPDA core is functionalized with GPx-mimicking SePh and SOD/CAT-mimicking MnO₂ for ROS scavenging and IR-1048 for enhanced NIR-II photothermal heating. TMB: 1,3,5-trimethylbenzene. (b) mPDA-SeMn-IR efficiently eliminates 6-OHDA-induced ROS to protect mitochondria, reduces α -synuclein expression, and restores neuronal functions. Photothermal activation of IP₃Rs in recovered neurons induces Ca²⁺ signaling, which upregulates tyrosine hydroxylase expression and activity and boosts dopamine release. (c) mPDA-SeMn-IR enables photothermal modulation of midbrain neurons and behavior control of zebrafish and exerts satisfactory therapeutic outcomes in the PD zebrafish model.

To minimize invasiveness in DBS, noninvasive wireless modalities including optical, 13 magnetic, 7 thermal, 14 and ultrasound-15based techniques have emerged for activating Ca²⁺ channels in targeted neurons through nanoactuatormediated energy transduction. Studies regarding noninvasive DBS for PD treatment are summarized in Table S1. Nonetheless, these approaches rely on viral transduction to introduce exogenous Ca2+ channels, which raise concerns regarding long-term safety, immune responses, and off-target effects. 16 Notably, dopaminergic neurons express endogenous Ca²⁺ channels, such as transient receptor potential vanilloid family member 1 (TRPV1), 17N-methyl-D-aspartate (NMDA) receptors, VGCC, and inositol 1,4,5-trisphosphate receptors (IP₃Rs), enabling nongenetic DBS strategies through endogenous Ca²⁺ channel manipulation. Our recent work demonstrates that photodriven nanoactuators can achieve precise

spatiotemporal regulation of IP_3R via in situ generation of agonists, effectively modulating neuronal excitability *in vivo*. ¹⁸ This proof-of-concept study indicates the therapeutic potential of IP_3R -targeted wireless stimulation for PD DBS treatment, which remains unexplored.

Despite its effectiveness, STN-DBS fails to arrest progressive neuronal degeneration, ultimately compromising long-term therapeutic outcomes, with 5-year postoperative quality-of-life scores falling to preoperative levels. The limitation arises from the reactive oxygen species (ROS) overproduction in PD pathogenesis, which mediates dopaminergic neurodegeneration. Growing evidence establishes that efficient ROS scavenging achieves superior neuroprotection, enabling partial reversal of neuronal functions. Therefore, integrating ROS scavenging into a DBS system would synergistically enhance the long-term efficacy of the DBS treatment.

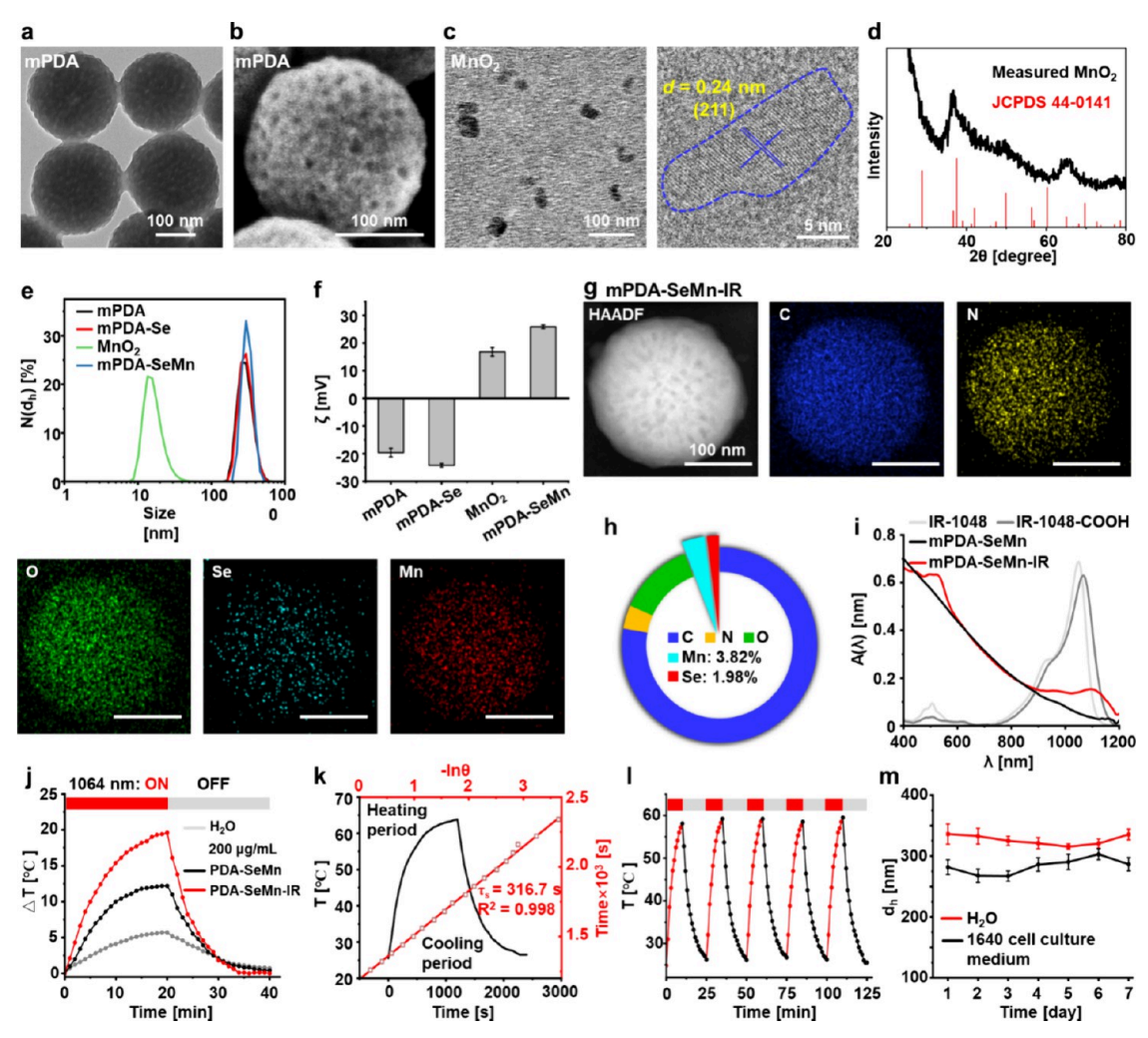


Figure 2. Characterizations of mPDA-SeMn-IR. (a) TEM and (b) SEM images of mPDA. (c) TEM image of MnO $_2$ showing (211) interplanar spacing of 0.24 nm. (d) PXRD patterns of MnO $_2$. (e) Hydrodynamic diameter d_h and (f) zeta potential ζ of mPDA, mPDA-Se, MnO $_2$, and mPDA-SeMn. (g) HAADF-STEM image and area-element mapping of mPDA-SeMn-IR. (h) Spectral analysis of data in (g) to measure the Mn and Se mass fractions. (i) Absorption of IR-1048, IR-1048-COOH, mPDA-SeMn, and mPDA-SeMn-IR aqueous solution. (j) Temperature changes of water, mPDA-SeMn, and mPDA-SeMn-IR (200 μ g/mL) over 20 min 1064 nm laser irradiation (1 W/cm 2), followed by 20 min cooling. (k) Time constant τ_s of mPDA-SeMn-IR for the heat transfer based on the linear time-dependent data collected during the cooling period. (l) Five cycles of photothermal heating of mPDA-SeMn-IR (200 μ g/mL) under 1064 nm laser irradiation (2 W/cm 2). (m) Changes in d_h of mPDA-SeMn-IR in water and 1640 cell culture medium over 1 week.

Here, we present an implant-free multifunctional nanoactuator that integrates wireless DBS with ROS scavenging for PD therapy. "Implant-free" denotes the elimination of both electrode implantation and genetic encoding by using NIR-II (second near-infrared window) photothermal activation of IP₃Rs through the incorporated NIR-II absorber IR-1048 (IR). As shown in Figure 1a, a mesoporous polydopamine (mPDA) core is encapsulated in a composite shell composed of 2-(phenylselanyl)ethan-1-amine (SePh) and manganese dioxide (MnO₂) to obtain an mPDA-SeMn-IR nanoparticle with dual therapeutic functionalities: (1) multienzyme-like ROS scavenging through glutathione peroxidase (GPx)-mimicking SePh and superoxide dismutase (SOD)/catalase (CAT)-mimicking MnO₂ and (2) IP₃Rs-mediated Ca²⁺ signaling enhancement for dopaminergic function. In vitro, mPDA-SeMn-IR protects PC-12 cells against 6-hydroxydopamine (6-OHDA)-induced neurotoxicity, activates IP₃Rs for Ca²⁺ signaling, upregulates tyrosine hydroxylase (TH) expression and activity, and boosts dopamine release (Figure 1b). In vivo, mPDA-SeMn-IR

enables photothermal neuromodulation and behavior control of zebrafish. PD zebrafish model further demonstrates restored dopaminergic neurons and improved locomotor behavior (Figure 1c). By combining noninvasive photothermal DBS with antioxidative capabilities without implants or genetic manipulation, this system offers a promising synergistic approach for PD management through simultaneous neural protection and modulation.

RESULTS

Syntheses and Characterizations of mPDA-SeMn-IR. mPDA served as an extensible platform for integrating multifunctional motifs to augment its antioxidant and photothermal ability. We chose mPDA over nonporous PDA for better functionalization and ROS scavenging. Spherical mPDA (transmission electron microscope (TEM)-measured diameter: 228.3 ± 15.6 nm) was prepared via dopamine self-polymerization in an ethanol/water mixture under alkaline conditions (Figure 1a and Figure S1). Porosity was induced

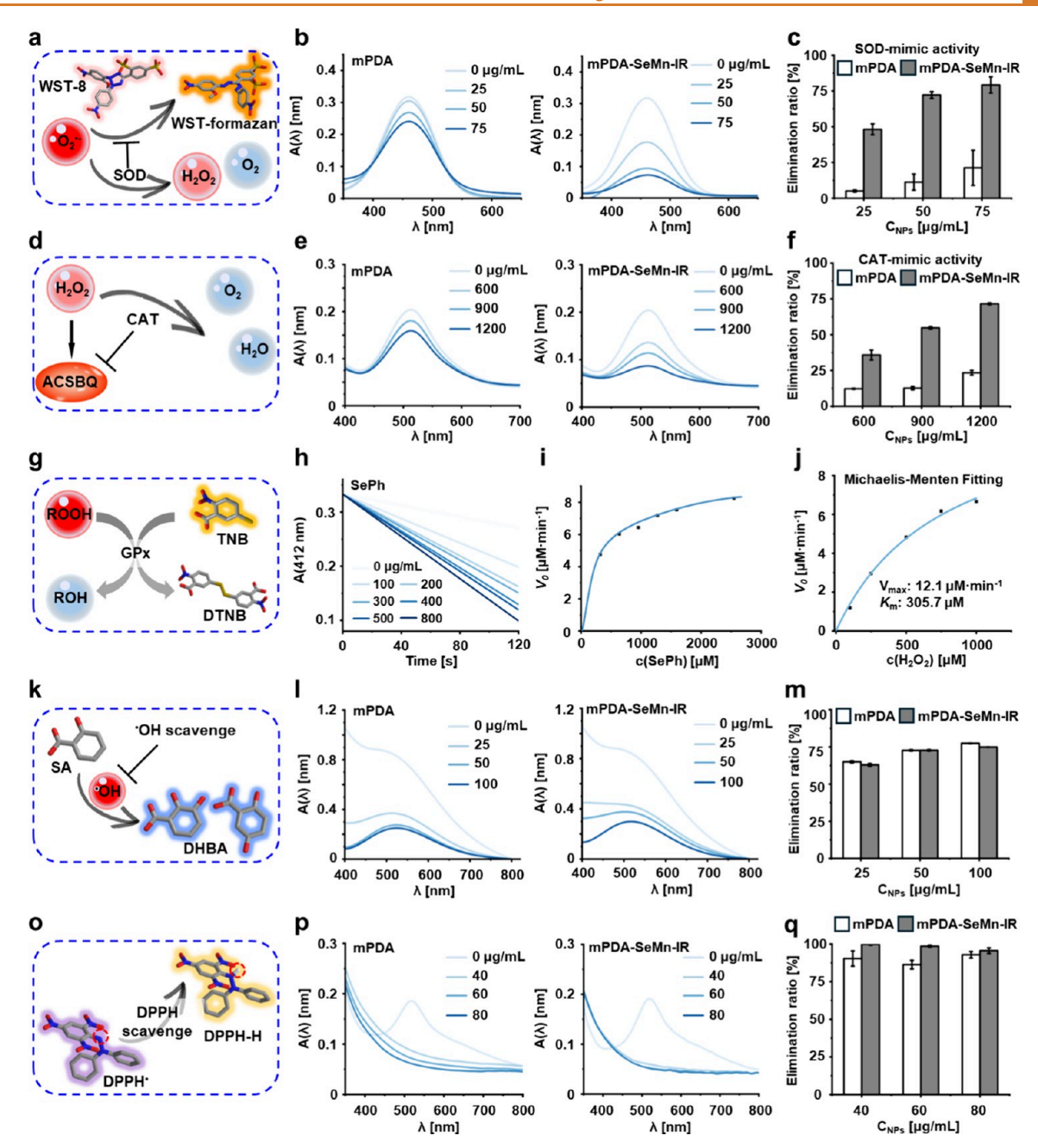


Figure 3. Multi-antioxidative properties of mPDA-SeMn-IR. (a) SOD-like activity detection via WST-formazan formation. (b) Absorption spectra of residual $O_2^{\bullet-}$ -induced generation of WST-formazan after incubation with mPDA-SeMn-IR and mPDA $(0-75\,\mu g/mL, 30\,min)$. (c) $O_2^{\bullet-}$ elimination ratios of both NPs. (d) CAT-like activity detection using the ACSBQ chromogenic system. ACSBQ: N-(4-antipyryl)-3-chloro-5-sulfonate-p-benzoquinone monoamine. (e) Absorption spectra of remaining H_2O_2 -induced formation of ACSBQ after incubation with both NPs $(600-1200\,\mu g/mL, 10\,h)$. (f) H_2O_2 decomposition efficiency. (g) GPx-like activity detection via TNB $(100\,\mu M)$ oxidation to DTNB. (h) Time-dependent absorbance changes of TNB $(100\,\mu M)$ with SePh $(0-800\,\mu g/mL)$. (i) Concentration-dependent initial reaction rates (V_0) derived from (h). (j) Michaelis—Menten kinetics of SePh $(300\,\mu g/mL)$ with TNB $(100\,\mu M)$ and H_2O_2 $(100-1000\,\mu M)$. (k) *OH scavenge detection via salicylic acid (SA) oxidation to dihydroxybenzoic acid (DHBA). (l) UV-vis absorption spectra of remaining *OH-induced formation of DHBA after incubation SA $(2\,mM)$ with both NPs $(0-100\,\mu g/mL, 30\,min)$. (m) *OH elimination efficiency. (o) Free radicals scavenge detection via DPPH* conversion to DPPH-H. p) DPPH* (purple) to DPPH-H (yellow) after incubation with both NPs $(0-80\,\mu g/mL, 30\,min)$. (q) DPPH* scavenging efficiency.

through the removal of Pluronic F-127-stabilized 1,3,5-trimethylbenzene micellar templates (Figure 2a,b). The Brunauer–Emmett–Teller (BET) surface area and average pore diameter of mPDA are 41.5 $\rm m^2/g$ and 18.9 nm, respectively. This surface area was 169.5-fold larger than nonmesoporous polydopamine nanoparticles (0.245 $\rm m^2/g$) of identical size (Figure S2). Functionalization with SePh via the

Michael addition/Schiff-base condensation reaction yielded mPDA-Se (Figures S3-S7).

MnO₂ was synthesized by reducing potassium permanganate (KMnO₄) with polyallylamine, ²⁶ whose interplanar spacing was 0.24 nm (Figure 2c), corresponding to the (211) plane of α -MnO₂. ²⁷ Powder X-ray diffraction (PXRD) displayed two broadened peaks at 37.2 and 66.1°, attributed to the (211) and

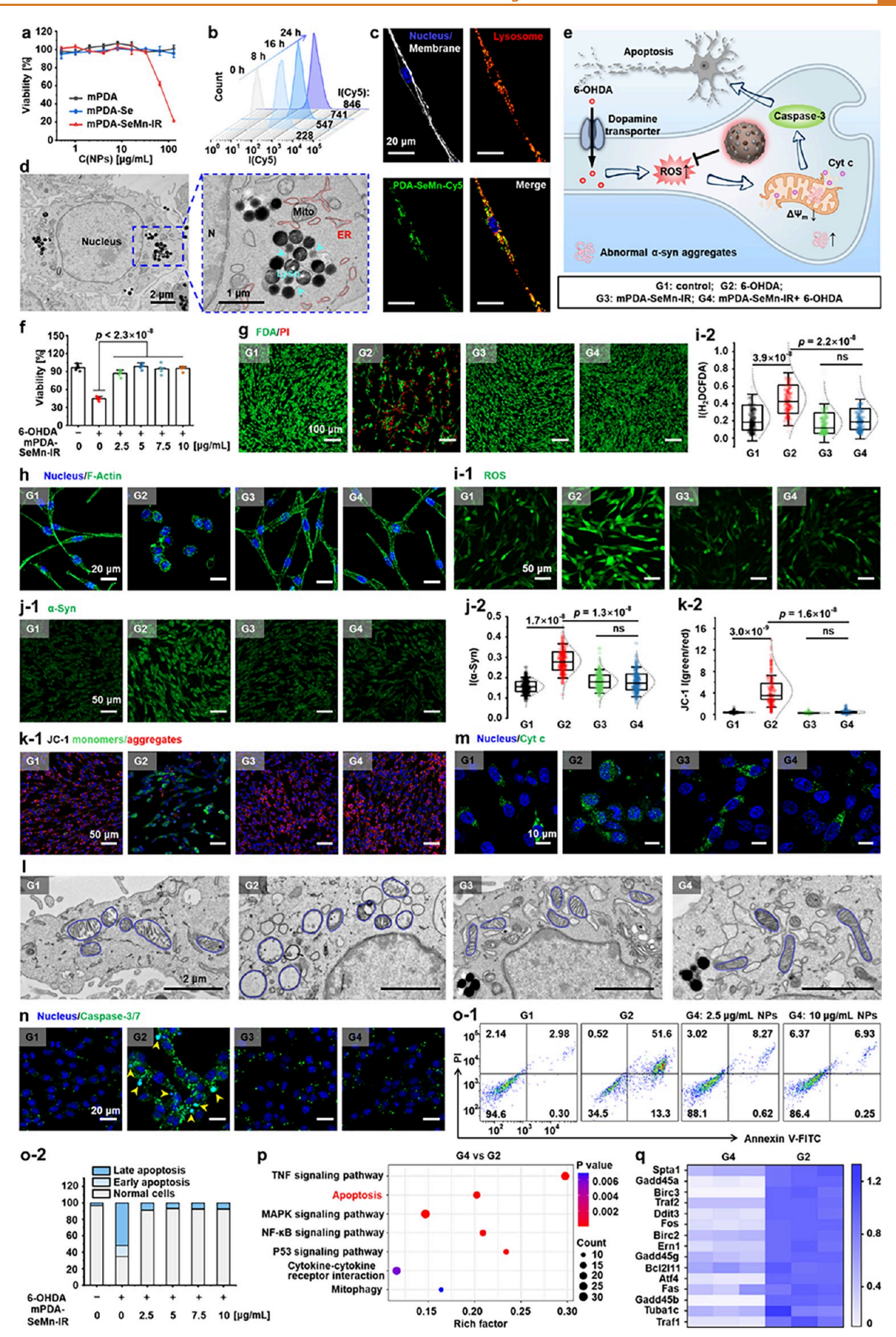


Figure 4. Neuroprotective effects and mechanisms of mPDA-SeMn-IR against the 6-OHDA-induced PD cell model. Unless specified, PC-12 cells were incubated with NPs (10 µg/mL) in serum-free culture medium for 24 h. (a) Dose-dependent cytotoxicity of mPDA, mPDA-Se,

Figure 4. continued

and mPDA-SeMn-IR. (b) Time-dependent cellular uptake of mPDA-SeMn-Cy5 as quantified by flow cytometry. (c) Confocal microscopy showing colocalization of mPDA-SeMn-Cy5 (green) and lysosomes (red). The nuclei stained with Hoechst 33342 are shown in blue. Plasma membrane stained with FITC-WGA is shown in gray. (d) BioTEM ultrastructural images of cells after incubation with mPDA-SeMn-IR. Mito: mitochondria; ER: endoplasmic reticulum (red lines); Lyso: lysosome (blue arrows). (e) Schematic of neuroprotective action of mPDA-SeMn-IR against 6-OHDA-induced neuronal damage. (f) Dose-dependent neuroprotection by mPDA-SeMn-IR against 6-OHDA (100 μ M) toxicity (n = 6 per group). (g) Live/dead assay measured by FDA/PI staining in various treatments. Live cells stained with FDA are shown in green. Dead cells stained with PI are shown in red. G1: control; G2:6-OHDA; G3: mPDA-SeMn-IR; G4: mPDA-SeMn-IR + 6-OHDA. (h) Confocal images of cell morphology after various treatments. F-actin stained with FITC-phalloidin is shown in green. Confocal images and quantification of (i) ROS levels (n > 204 cells per group), (j) α -syn expression (n > 301 cells per group), (k) JC-1 staining (n > 389 cells per group), (m) cytosolic Cyt c release, and (n) caspase-3/7 activity after different treatments. (l) BioTEM images showing changes in mitochondrial morphology (blue outlines). (o-1) Flow cytometry results of cell apoptosis measured by FITC-Annexin V/PI assay and (o-2) ratios of normal, early apoptotic, and late apoptotic cells. (p) KEGG pathway enrichment analysis exhibiting apoptosis and apoptosis-related pathways in 6-OHDA + mPDA-SeMn-IR versus 6-OHDA comparison. (q) Heatmap of downregulated apoptosis-related genes in the KEGG pathway.

(002) planes of α -MnO $_2$ (JCPDS44-0141) with poor crystallinity ²⁸ (Figure 2d). Dynamic light scattering (DLS) revealed a hydrodynamic diameter $d_{\rm h}$ of 15.8 \pm 0.1 nm and a zeta potential ζ of 16.8 \pm 1.7 mV (Figure 2e,f). MnO $_2$ was then electrostatically absorbed onto mPDA-Se ($d_{\rm h}$: 297.2 \pm 1.6 nm, ζ : -19.6 \pm 1.5 mV) to afford mPDA-SeMn, which exhibited a slightly larger size ($d_{\rm h}$: 310.7 \pm 1 nm) and positive charge (ζ : 25.9 \pm 0.6 mV, Figure 2e,f). High-angle annular dark field scanning transmission electron microscopy (HAADF-STEM) images and area-elemental mapping confirmed homogeneous Se and Mn distributions throughout the composite (Figure 2g). The spectral analysis showed Mn and Se mass fractions of 3.82 and 1.98%, respectively (Figure 2h), which matched inductively coupled plasma mass spectrometry data (ICP-MS, Mn: 3.05%, Se: 2.08%, Figure S8).

As both MnO₂ and mPDA had low NIR-II absorbance (Figure S9), IR-1048 was covalently conjugated via reaction with its N-hydroxysuccinimide (NHS) ester and polyallylamine on mPDA-SeMn (Figure S10), yielding mPDA-SeMn-IR. New peaks at 520 and 1100 nm with a slight red shift relative to IR-1048-COOH verified successful conjugation (Figure 2i). Under 1064 nm irradiation (1 W/cm², 20 min), mPDA-SeMn-IR demonstrated superior photothermal heating over mPDA-SeMn (Figure 2j and Figure S11a), with temperature elevation positively correlated with laser power (Figure S11b). Photothermal conversion efficiency (η) calculations derived from thermal equilibrium time constants (τ_s) revealed $\eta = 61.0\%$ for mPDA-SeMn-IR (Figure 2k), surpassing reported photothermal nanosystems, like the gold nanorod@PDA (40%)²⁹ and gold nanostar@metal-organic frameworks (30.2%).³⁰ Additionally, five consecutive heating/ cooling cycles maintained constant maximum temperatures, demonstrating excellent thermostability (Figure 21). mPDA-SeMn-IR preserved the morphology of mPDA after the integration of all functional motifs (Figure S12). DLS results confirm its high colloidal stability in both water (for storage) and cell culture medium (for cell experiments) over 1 week (Figure 2m), which is beneficial for biological applications.

Evaluation of Multienzymatic Catalytic Activity and ROS Scavenging Capability. The intracellular antioxidant system maintains ROS homeostasis through enzymes (e.g., SOD, CAT, and GPx) and nonenzymatic reductants. The mPDA-SeMn-IR mimicking biological antioxidant process was anticipated to outperform mPDA. Specifically, the cascade SOD/CAT-like activities first catalyzed the dismutation of superoxide radical $(O_2^{\bullet-})$ into O_2 and H_2O_2 , followed by H_2O_2 decomposition into H_2O and O_2 . Concentration-

dependent scavenging assays revealed that mPDA-SeMn-IR (75 μ g/mL) removed 79.2% of the $O_2^{\bullet-}$ produced by the xanthine—xanthine oxidase (3.73-fold higher than mPDA, Figure 3a—c) and degraded 71.6% of H_2O_2 (3.06-fold more efficient than mPDA, Figure 3d—f).

As a GPx mimic, SePh catalyzes hydroperoxide (ROOH, R = H/alkyl) reduction to ROH via glutathione (GSH) oxidation into glutathione disulfide (GSSG). GPx-like activity was quantified using the 2-nitro-5-sulfanylbenzoic acid (TNB) assay, where yellow TNB is converted to colorless 5,5-dithiobis(2-nitrobenzoic acid) (DTNB) (Figure 3g). Figure 3h shows the decrease in absorbance corresponding to an elevation in SePh concentrations. As the SePh concentration increased, the reaction rates initially escalated and then plateaued, demonstrating characteristic saturation kinetics of enzymatic reactions (Figure 3i). Michaelis-Menten kinetics were confirmed by varying H2O2 concentrations at a fixed SePh concentration (300 μ g/mL) with substrate concentration-dependent velocity profiles (Figure 3j and Figure S13). Notably, SePh exhibited superior catalytic efficiency (8.0 × $10^{-3} \mu M/min/\mu M$), far exceeding other GPx mimics (e.g., PhSeSePh: $2.4 \times 10^{-5} \, \mu \text{M/min/} \mu \text{M}$).³²

Reducing mPDA can directly scavenge hydroxyl radical (${}^{\bullet}$ OH) through hydroxylation of its 5,6-dihydroxyindole structural units.³³ Using the salicylic acid (SA)—dihydroxybenzoic acid (DHBA) chromogenic system (Figure 3k), both mPDA-SeMn-IR and mPDA (100 μ g/mL) exhibited comparable ${}^{\bullet}$ OH scavenging performance (75%, Figure 3l,m). Given the role of elevated reactive nitrogen species (RNS) in PD pathogenesis,³⁴ we chose 2,2-diphenyl-1-picrylhydrazyl radical (DPPH ${}^{\bullet}$) as free radicals to test RNS scavenging ability²¹ (Figure 3o). Remarkably, both NPs eliminated almost >90% DPPH ${}^{\bullet}$ at all tested concentrations (Figure 3p,q). Collectively, these results validate the multi-antioxidative nature of mPDA-SeMn-IR for potential PD intervention.

Interactions with Cells and Neuroprotective Effects of mPDA-SeMn-IR. The neurotoxicity profile and cellular processing of mPDA derivatives were systematically investigated in differentiated PC-12 cells, a rat adrenal pheochromocytoma neurogenic cell known for dopamine synthesis. While mPDA and mPDA-Se exhibited excellent biocompatibility (>95% at 128 μ g/mL, 24 h), mPDA-SeMn-IR resulted in less than 60% viability at concentrations above 64 μ g/mL (Figure 4a). This differential toxicity originates from two faces of MnO₂: despite its remarkable SOD/CAT-like properties, excessive MnO₂ triggers GSH depletion (MnO₂ + GSH \rightarrow GSSH + Mn²⁺) and Fenton-like reaction (Mn²⁺ + H₂O₂ \rightarrow

Mn³+ + •OH + OH¯).³5 Therefore, 10 μ g/mL was selected as the optimal dose for subsequent studies. Flow cytometry revealed the time-dependent cellular uptake of Cy5-labeled mPDA-SeMn (Figure 4b). Confocal imaging displayed over 55% colocalization (yellow puncta) between mPDA-SeMn-Cy5 (green) and lysosomes (red; Figure 4c and Figure S14). BioTEM data further confirmed the accumulation of several mPDA-SeMn-IR NPs in a large lysosome (Figure 4d).

The neuroprotective efficacy of mPDA derivatives was evaluated in a 6-OHDA-induced PD cellular model. Mechanistically, 6-OHDA enters dopaminergic neurons via dopamine transporters, elevates ROS production, and disrupts mitochondrial complex I activity, recapitulating PD pathophysiology³⁶ (Figure 4e). PC-12 cells were incubated with 6-OHDA (100 μ M) alone or with mPDA, mPDA-Se, and mPDA-SeMn-IR. To quantify the neuroprotective effect, we defined the "protection index" as [(V(NP + 6-OHDA) - V(6-OHDA))/ $V(6\text{-}OHDA)] \times 100\%$, where V indicates cell viability. Notably, mPDA-SeMn-IR (10 μ g/mL) fully protected cells, achieving a 112.9% protection index, outperforming mPDA (35.5%) and mPDA-SeMn (61.8%) (Figure 4f and Notes S2). Fluorescein diacetate/propidium iodide (FDA/PI) live/dead assays confirmed these findings, showing minimal cell death in the mPDA-SeMn-IR group (Figure 4g). Moreover, cell morphology changes were compared by staining F-actin filaments with FITC-phalloidin. 6-OHDA caused cytoskeletal collapse (rounded cells and retracted neurites), whereas mPDA-SeMn-IR preserved neuronal integrity, maintaining a spindle-shaped morphology with extended neurites (Figure 4h). The effect of mitotic rounding was excluded, as flow cytometric cell cycle analysis revealed slight G2/M phase elevation in 6-OHDA groups (19.6 \pm 0.5%) versus the control $(16.9 \pm 0.8\%, Figure S16).$

We further explored the degradation of mPDA-SeMn under physiologically relevant oxidative conditions. mPDA-SeMn exhibited H₂O₂ concentration-dependent degradation kinetics. UV—vis absorbance of the NP solution decreased slightly at 0.5 mM H₂O₂ but moderately at 8 mM H₂O₂ (Figure S17a,b). TEM analysis showed surface fragmentation without size alteration at 0.5 mM H₂O₂, whereas 8 mM H₂O₂ caused extensive fragmentation, particle fusion, and significant diameter reduction (203.0 nm vs initial 231.5 nm, Figure S17c,d). The slower degradation kinetics of mPDA-SeMn versus conventional PDA^{37,38} was attributed to CAT-mimic activity of MnO₂. Following 3-day incubation in 6-OHDA-treated PC-12 cells, particle debris was observed in lysosomes and the diameter reduced to 208.9 nm, while mesoporous architecture remained preserved (Figure S17e).

Verification of Neuroprotective Mechanisms. Heightened oxidative stress, abnormal aggregation of α -synuclein (α -syn), and consequent mitochondrial impairment constitute primary drivers of neurodegeneration. 6-OHDA raised intracellular ROS levels by 2.5-fold, as measured by 2',7'-dichlorodihydrofluorescein diacetate (H₂DCFDA) fluorescence intensity I(H₂DCFDA) (Figure 4i). In PC-12 cells, 10 μ g/mL MnO₂ significantly increased oxidative stress and decreased GSH/GSSG ratios, whereas 1 μ g/mL MnO₂ showed no significant effect versus the control (Figure S18a,b). ICP data showed that 10 μ g/mL of mPDA-SeMn-IR contained only 0.604 μ g/mL MnO₂, a concentration insufficient to induce measurable redox disruption. In 6-OHDA-treated PC-12 cells, all formulation significantly reduced ROS and increased GSH/GSSG ratios vs 6-OHDA controls. ROS

scavenging efficiency ranked as mPDA-SeMn-IR > mPDA-Mn > mPDA-Se > mPDA (Figure 4i and Figure S18a,b). Critically, PhSe-containing formulations (mPDA-Se and mPDA-SeMn-IR) exhibited lower GSH/GSSG ratios than nonselenized counterparts (mPDA and mPDA-Mn) (Figure S18c), as GPx-mimetic PhSe converted H_2O_2 to H_2O at the cost of oxidizing GSH to GSSG. The antioxidant capacity was further validated using the Rosup-induced model (Figure S19).³⁹ Despite controversy about the role of α -syn in 6-OHDA-induced PD models, accumulating evidence from *in vitro* and *in vivo* studies confirms the involvement of α -syn overexpression and aggregation.^{40–43} Immunofluorescence staining revealed that mPDA-SeMn-IR significantly suppressed 6-OHDA-induced α -syn upregulation (Figure 4j-1,j-2).

Subsequently, mitochondrial integrity was systematically evaluated. JC-1 probe quantification revealed 6-OHDAinduced mitochondrial membrane potential collapse, evidenced by a 11.8-fold increase in the JC-1 green-to-red intensity ratio I(green/red) versus control, whereas mPDA-SeMn-IR treatment reversed to baseline levels (Figure 4k-1,k-2). BioTEM ultrastructural analysis showed that mPDA-SeMn-IR preserved mitochondrial cristae architecture, countering 6-OHDA-induced matrix swelling and cristae fragmentation (Figure 4l). Cytochrome c (Cyt c), a marker protein in the mitochondrial inner membrane, is released into the cytoplasm as a result of increased mitochondrial membrane permeability, thereby inducing intrinsic apoptosis. Immunofluorescence staining revealed preservation of mitochondrial Cyt c localization in mPDA-SeMn-IR-treated cells, showing characteristic punctate fluorescence (mitochondrial retention) versus 6-OHDA-induced diffusive and faint cytosolic distributions (Figure 4m). Furthermore, the activity of downstream apoptotic effectors, Caspase-3/7, was evaluated using the Caspase-3/7 Green Detection Reagent. The rationale is that caspase-3/7 cleaves GreenNuc from weakly fluorescent DEVD-GreenNuc conjugates, which binds DNA to generate strong fluorescence. 6-OHDA-treated cells exhibited pronounced GreenNuc fluorescence, with some cells showing intense intranuclear accumulation (indicated by yellow arrows), whereas the mPDA-SeMn-IR group had markedly reduced fluorescence (Figure 4m). Flow cytometry quantification via FITC-Annexin V/PI staining demonstrated the potent antiapoptotic capacity of mPDA-SeMn-IR, dramatically reducing the apoptotic ratio from 64.9% (6-OHDA) to 8.9% at a concentration of 2.5 μ g/mL (Figure 40-1,0-2 and Figure S20).

To investigate the molecular mechanisms underlying the therapeutic effects, transcriptome sequencing was performed on PC-12 cells subjected to 6-OHDA and 6-OHDA + mPDA-SeMn-IR treatments. Kyoto Encyclopedia of Genes and Genomes (KEGG) pathway enrichment analysis revealed that apoptosis and its related pathways were closely correlated with the therapeutic mechanism of mPDA-SeMn-IR (Figure 4p). Specifically, 15 key apoptosis-related genes were remarkably downregulated in the presence of mPDA-SeMn-IR (Figure 4q). These transcriptional changes were consistent with observed phenotypic improvements, collectively demonstrating that mPDA-SeMn-IR effectively mitigated oxidative stress, suppressed α -syn expression, and preserved mitochondrial integrity to inhibit apoptosis execution.

Photothermal Modulation of Cell Ca²⁺ Response. Photothermal modulation of Ca²⁺ signaling was tested by incubating PC-12 cells with mPDA-SeMn-Cy5/mPDA-SeMn-

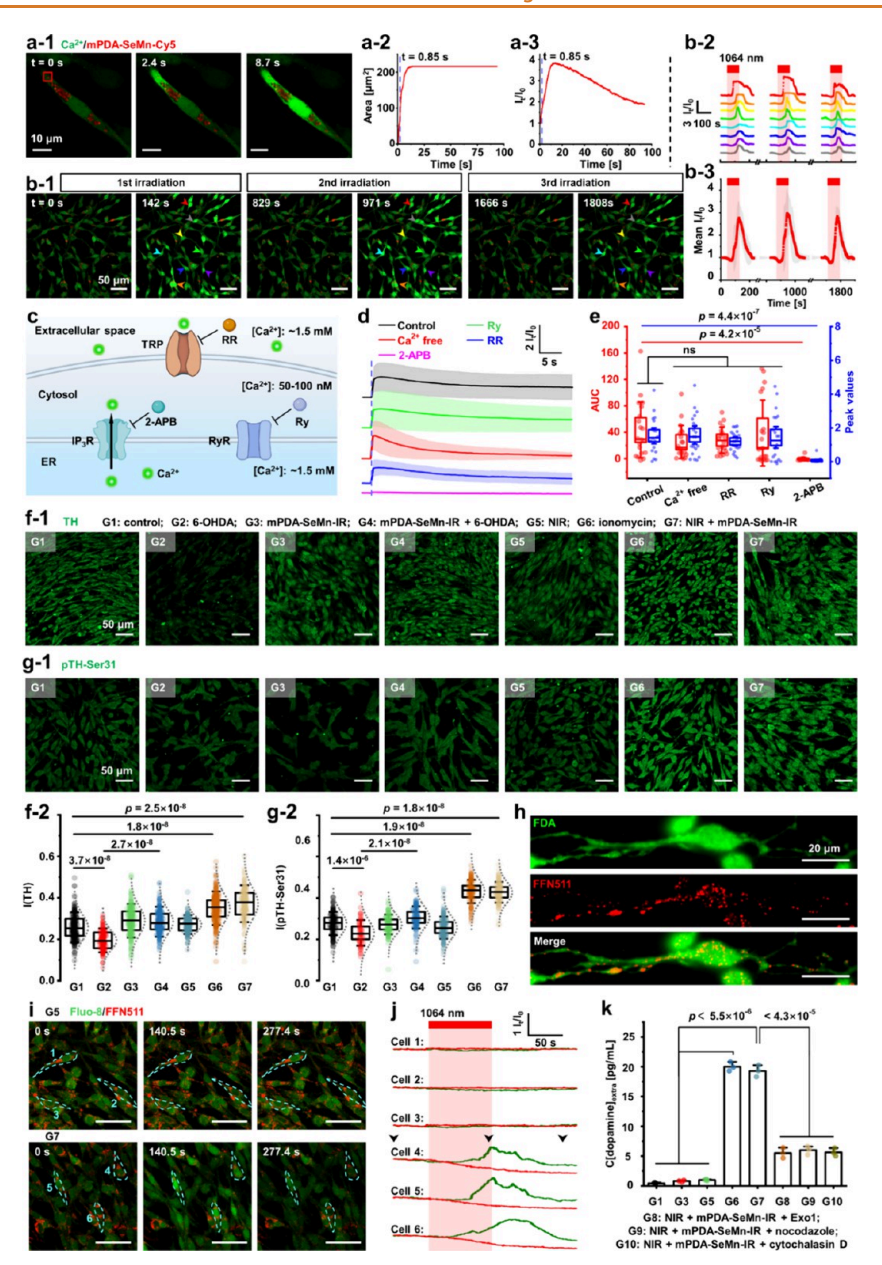


Figure 5. Photothermal Ca²⁺ activation for enhanced dopamine biosynthesis and release. (a-1) Single-cell Ca²⁺ dynamics upon photoexcitation by confocal laser (488 nm, 2.27 mW, 0.16 s). The red box indicates the photoexcited region. Ca²⁺ indicated by Fluo-8 is shown in green. mPDA-SeMn-Cy5 is shown in red. (a-2,3) Spatiotemporal Ca²⁺ propagation quantified as propagated area and normalized intensity I_t/I_0 . (b-1) Repetitive stimulation of multiple cells using a 1064 nm laser (2 W/cm², 90 s). (b-2) Time-dependent I_t/I_0 of eight cells indicated by arrows and (b-3) the mean I_t/I_0 values. Shading represents the standard derivative. (c) Schematic illustration depicting possible Ca²⁺ entry pathways into the cytosol. (d) Normalized Ca²⁺ transients in control, Ca²⁺-free medium, RR (30 μ M), Ry (25 μ M), and 2-APB (100 μ M) treated groups. (e) AUC and peak I_t/I_0 (n = 25 cells per group). ns: not significant. Immunofluorescence images of (f) TH (n > 289 cells per group) and (g) pTH-Ser31 (n > 183 cells per group) under different treatments. G1: control; G2:6-OHDA; G3: mPDA-SeMn-IR; G4: mPDA-SeMn-IR + 6-OHDA; G5: NIR; G6: ionomycin; G7: NIR + mPDA-SeMn-IR. (h) FFN511 (red) vesicle distribution. Cytosol stained with FDA is shown in green. (i) Dopamine release from cells as indicated by decreased I(FFN551) in G5 and G7. (j) Time-dependent I_t/I_0 (Fluo-8) and I_t/I_0 (FFN511). (k) Extracellular dopamine concentrations after different treatments (n = 3 per group). G8: NIR + mPDA-SeMn-IR + Exo1; G9: NIR + mPDA-SeMn-IR + nocodazole; G10: NIR + mPDA-SeMn-IR + cytochalasin D.

IR for 24 h and stained with Ca^{2+} indicator Fluo-8. Localized photoexcitation of mPDA-SeMn-Cy5 (indicated by a red box) using the confocal laser (488 nm, 2.27 mW, 0.16 s) triggered a rapid Ca^{2+} response (<0.35 s), as evidenced by Fluo-8 fluorescence intensity I(Fluo-8) elevation surrounding the irradiated NPs (Figure 5a-1 and Video 1). Ca^{2+} wave propagated throughout the cell and reached maximum I(Fluo-8) within 9.4 s (Figure 5a-2,a-3). Subsequent Ca^{2+}

clearance via plasma membrane pump extrusion and endoplasmic reticulum (ER) reuptake restored baseline fluorescence within several minutes (Figure 5a-3). Sequential irradiation of different NPs enabled repetitive cell Ca^{2+} activation up to six times (Figure S21). In addition to confocal laser, a 1064 nm laser pointer (2 W/cm², 90 s) could induce three successive Ca^{2+} responses with a 30 s delay (Figure 5b and Video 2).

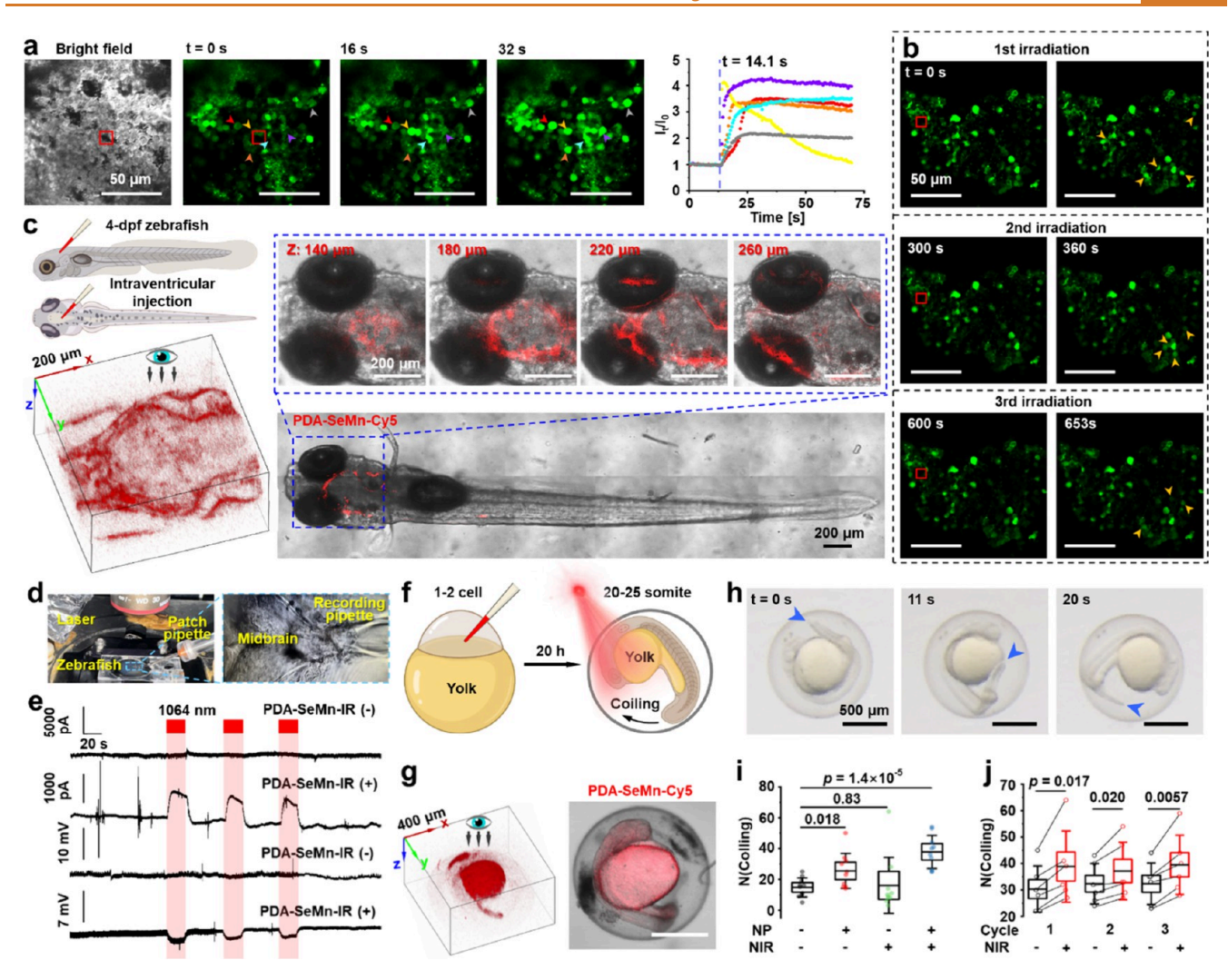


Figure 6. Photothermal DBS for regulating coiling behavior. (a) Ca²⁺ activation in *ex vivo* brain. Membrane-associated mPDA-SeMn-IR indicated by the red box were irradiated by the confocal laser (2.27 mW, 0.16 s). (b) Repetitive stimulation of the *ex vivo* brain to activate distant neurons. (c) 3D reconstruction and z-stack images of mPDA-SeMn-Cy5 fluorescence in 4-dpf (days post fertilization) zebrafish brain after intraventricular microinjection. (d) Setup for *in vivo* recording of the local field voltage/current in the brain during photothermal activation. (e) Electrophysiological activity of neurons stimulated by three cycles of 1064 nm laser (2 W/cm², 20 s) illumination. (f) Schematic of establishing zebrafish model for coiling assay. (g) 3D reconstruction of mPDA-SeMn-Cy5 fluorescence in the embryonic zebrafish at 20–25 somite stage. (h) Snap photos of coiling movement of an embryonic zebrafish during the 1064 nm laser irradiation. Arrows indicated the tail. (i) Coiling times N(coiling) of embryonic zebrafish under different treatments in 3 min observation (n = 10 per group). (j) N(coiling) of embryonic zebrafish in three 3 min on/3 min off laser cycles (n = 6 per group).

We next investigated the Ca²⁺ activation mechanism. A steep Ca²⁺ gradient exists between cytosol (Ca²⁺ concentration: 50– 100 nM), extracellular space, and ER (both ~1.5 mM), allowing Ca²⁺ entry from both locations (Figure 5c). The proximity of internalized mPDA-SeMn-IR to the ER suggested photothermal activation of ryanodine receptors (RyRs) or IP₃Rs on the adjacent ER (Figure 4d,l). To verify this hypothesis, Ca²⁺ outside cells were depleted or Ca²⁺ channels were blocked before confocal photoexcitation. The inhibition was quantified by the reduction in the area under the curve (AUC) and peak values. Extracellular Ca²⁺ depletion, inhibition of thermosensitive transient receptor potential (TRP) (30 µM ruthenium red, RR), or RyRs blocking (25 μM ryanodine, Ry) cannot significantly attenuate Ca²⁺ responses (Figure 5d,e). In sharp contrast, IP₃R blockade (100 µM 2-aminoethyl diphenylborinate, 2-APB) significantly reduced both AUC and peak values by over 95%, establishing IP₃R as the primary photothermally activated target. Our prior

work demonstrated that photothermal disruption of micronsized lysosomes could initiate lysosomal Ca^{2+} -mediated Ca^{2+} release, thereby amplifying cytosolic Ca^{2+} signals. To investigate potential lysosomal Ca^{2+} involvement, we performed sequential experiments in the same cell: (i) first, confocal laser photoexcitation triggered robust cytosolic Ca^{2+} elevation (Figure S22a); (ii) subsequent addition of thapsigargin (a sarco/ER Ca^{2+} adenosine triphosphatase inhibitor) depleted ER Ca^{2+} stores by preventing Ca^{2+} reuptake to ER (Figure S22b); and (iii) photoexcitation of other mPDA-SeMn-RhB-containing lysosomes failed to cause a detectable increase in I(Fluo-8) surrounding irradiated lysosome (Figure S22c). These results demonstrated that lysosomal Ca^{2+} release was not the key factor triggering the cell Ca^{2+} response.

Other photothermal modulation mechanisms include membrane capacitance change-induced transient capacitive current 45 and ER Ca²⁺ outflow-uptake imbalance during

cooling. ⁴⁶ Capacitive current generation necessitates ultrafast thermal transients $(dT/dt > 10^3 \text{ K/s})$, ^{47,48} which was not the case in our study. Figure 5b shows decreased I(Fluo-8) during the cooling phase, excluding the second mechanism. Collectively, these findings revealed that localized photothermal heating directly activated IP₃Rs, initiating focal Ca²⁺ release that propagated via Ca²⁺-induced Ca²⁺ release (CICR) through adjacent ER domains, leveraging endogenous amplification pathways for Ca²⁺ signaling propagation.

Ca²⁺ Signaling Upregulated TH Expression and Activity, Dopamine Biosynthesis, and Release. TH, the rate-limiting enzyme in dopamine biosynthesis, ⁴⁹ constitutes a pathological hallmark of PD through its characteristic deficiency. Membrane depolarization-induced Ca2+ influx through VGCC is the primary driver of TH upregulation, phosphorylation (typically at serine residues Ser40 or Ser31), and dopamine exocytosis (details are summarized in Table S2). Both upregulated TH expression and its phosphorylationactivated catalytic capacity potentiate dopamine biosynthesis. Our photothermal modulation of ER Ca²⁺ efflux replicated these regulatory mechanisms. Immunofluorescence quantification revealed that 6-OHDA-lesioned cells reduced 24 and 17% of TH and pTH-Ser31 levels versus controls, respectively, whereas mPDA-SeMn-IR entirely restored them (Figure 5f,g). Remarkably, 24 h NIR-II irradiation (2 W/cm², 60 s, nine times) elevated TH and pTH-Ser fluorescence by 44 and 54%, respectively, matching Ca²⁺ ionophore (ionomycin) efficacy. Laser-only treatment produced no significant alterations. Correspondingly, photothermal activation of PC-12 cells significantly increased dopamine biosynthesis, elevating both intracellular and secreted dopamine levels by 1.2-fold relative to the control and mPDA-SeMn-IR-only groups. This enhancement approached the efficacy of ionomycin treatment (1.27-fold increase vs control; Figure S23). We proposed that ER Ca²⁺ release activates Ca²⁺-sensitive forms of adenylyl cyclase, generating cyclic adenosine monophosphate (cAMP) to stimulate protein kinase A (PKA). Concurrently, elevated cytosolic Ca²⁺ activates calmodulin (CaM) kinase. Both kinases phosphorylate CREB to form pCREB, which transactivate TH transcription by binding the cAMP/Ca²⁺ response element (CRE/CaRE) in the promoter region for upregulated TH expression. 50,51 Subsequently, PKA and associated kinases phosphorylate TH at Ser31/Ser40 residues, converting the enzyme to its catalytically active form. 52,53 This cascade integrates Ca2+ signaling with TH regulation through coordinated transcriptional and post-translational control (Figure S24).

FFN511, a fluorescent false neurotransmitter residing in synaptic dopamine vesicles,⁵⁴ was utilized to visualize dopamine exocytosis. Punctate FFN511 signals were distributed throughout soma and neurites (Figure 5h). Photothermal activation (1064 nm, 2 W/cm², 90 s) evoked simultaneous I(Fluo-8) elevation and I(FFN511) attenuation, indicating Ca²⁺-mediated vesicular dopamine release (Figure 5i,j and Video 3). Figure S25 further demonstrates progressive attenuation in both the soma and neurite of PC-12 cells. These results are consistent with previous reports that nigrostriatal neurons release dopamine from their somata and dendrites in the substantia nigra pars compacta and pars reticulata, and from axons in striatum. 55 The extracellular dopamine concentration ($C[dopamine]_{extra}$) was quantified by an electrochemical workstation (Figure S26). Photothermal treatment increased C[dopamine]_{extra} to 17.8 pg/mL, while neither laser

nor NPs alone had any effect (Figure 5k). Pharmacological validation confirmed exocytic mechanisms: 2-(4-fluorobenzoylamino)benzoic acid methyl ester (Exo1, an exocytic pathway inhibitor), 56 nocodazole (a microtubule-depolymerizing reagent to prevent exocytic vesicle transport), and cytochalasin D (a F-actin filament-depolymerizing reagent to inhibit fusion pore opening) 57,58 significantly reduced C[dopamine]_{extra} to 27.5, 30.0, and 28.2% versus NIR + mPDA-SeMn-IR group, respectively. This result aligns with the report by Rice et al., where IP₃R-gated ER Ca²⁺ release facilitated somatodendritic dopamine release from nigrostriatal neurons in the substantia pars compacta in guinea pigs. 55 These findings establish photothermal ER Ca²⁺ release as a dual regulator of dopamine biosynthesis and release.

Photothermal Neuromodulation to Regulate Coiling Behavior of Embryonic Zebrafish. Nongenetic optical neural modulation enables precise circuit control for behavioral manipulation and neurological therapy. 17,18,48,59,60 To activate zebrafish brain neurons, the ex vivo brains were incubated with mPDA-SeMn-IR (10 μ g/mL) and Fluo-8. Given the small size of neurons (soma diameter: $4-6 \mu m$), NPs clustered on the cell membrane rather than being internalized. Photoexcitation by the confocal laser (2.27 mW, 0.16 s) evoked Ca²⁺ transients both proximally and distally from stimulation sites (Figure 6a). The repetitive activation of distal neurons (Figure 6b) demonstrates the feasibility of neural network activation through interneuronal communication without the need to directly stimulate all neurons simultaneously. The 1064 nm laser could also repeatedly activate ex vivo brain (2 W/cm², 60 s, Figure S27). For in vivo stimulation, intraventricular NP administration achieved brain surface deposition without spinal cord or brain infiltration (Figure 6c). The half-life of intraventricularly microinjected mPDA-SeMn-RhB in zebrafish was about 41.7 h based on fluorescence decay kinetics (Figure S28). Electrophysiological recordings via intracranial pipettes revealed that NIR-II triggered (2 W/cm², 20 s) reproducible local field voltage/current signals in the presence of mPDA-SeMn-IR (Figure 6d,e). These results confirmed successful photothermal neuromodulation.

Embryonic zebrafish provide an ideal model for optical neuromodulation due to their optical transparency and quantifiable motor outputs (e.g., coiling). Following microinjection of mPDA-SeMn-IR (12.5 ng) at the 1-2 cell stage (24 h survival: 100% Table S5; 13-day survival: 95% Table S6), coiling behavior was examined at the 20-25 somite stage (Figure 6f). mPDA-SeMn-Cy5 NPs were predominantly accumulated in yolk with others distributed in the brain (Figure 6g). Photothermal activation of brain motor cells can generate motor output.⁶¹ Coiling behavior was monitored with an optical microscope, where each coiling event involved embryo dragging and tail rounding (Figure 6h). Quantification of coiling times during 3 min of observation showed that photothermal stimulation induced 2.24-fold higher activity versus controls (38 vs 17 coils) (Figure 6i). NP-injected zebrafish were then subjected to three consecutive 3 min on/3 min off laser cycles. Consistently, NIR-II laser stimulation significantly increased coiling compared with the laser-off condition (Figure 6j and Video 4).

Alleviating Parkinsonian Symptoms in the Zebrafish PD Model. Finally, the therapeutic effects of mPDA-SeMn-IR were investigated in a 6-OHDA-induced zebrafish PD model. mPDA-SeMn-IR effectively eliminated 6-OHDA-induced ROS by 70% in the *ex vivo* brain (Figure 7a). To establish a

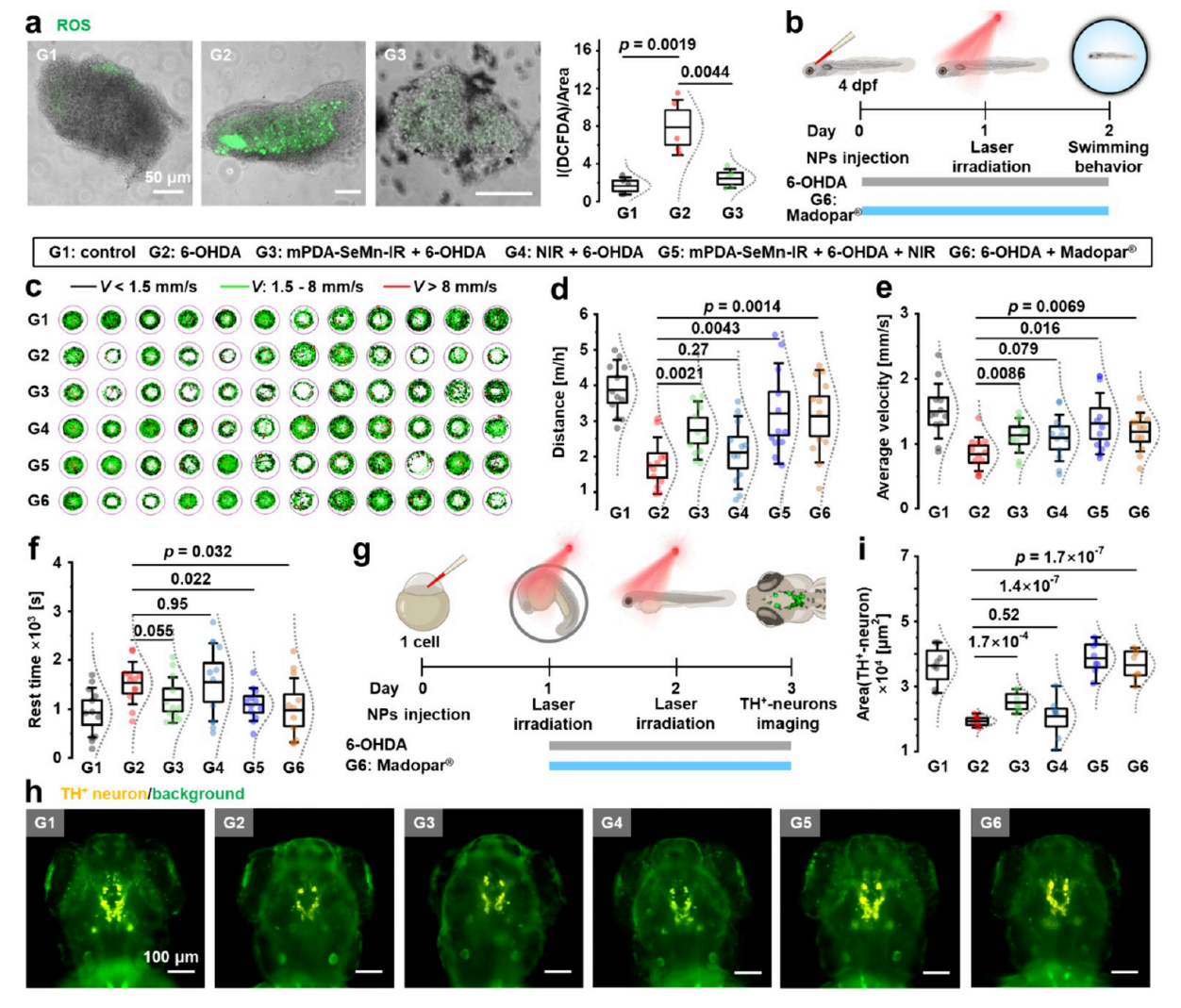


Figure 7. Therapeutic effects of mPDA-SeMn-IR in alleviating Parkinsonian symptoms in the zebrafish PD model. (a) ROS levels of ex vivo brain after three treatments (n=5 per group). G1: control; G2:6-OHDA; G3: mPDA-SeMn-IR + 6-OHDA. (b) Timeline of establishing the zebrafish PD model for the open-field swimming test. 4-dpf zebrafish were intraventricularly injected with mPDA-SeMn-IR or extracellular solution and then exposed to 6-OHDA ($250 \mu M$). After different treatments, the swimming behavior on day 2 was assessed. G4: NIR + 6-OHDA; G5: mPDA-SeMn-IR + 6-OHDA + NIR; G6: Madopar. (c) Trajectories and speed of zebrafish within 1 h of observation (n=12 per group). The (d) swimming distance, (e) average velocity, and (f) rest time of zebrafish in each group. (g) Timeline of establishing the zebrafish PD model for measuring TH⁺ neuron. TH-P2A-EGFP knock-in zebrafish were injected with mPDA-SeMn-IR or extracellular solution at the 1-2 cell stage and then exposed to 6-OHDA ($250 \mu M$) at 1 dpf. After different treatments, TH⁺ neuron on day 3 was assessed. (h) Fluorescence images of midbrain TH⁺ neurons (yellow) and (i) quantified area (n=8 per group). Other tissues are shown in green.

zebrafish PD model, 4-dpf zebrafish were intraventricularly injected with mPDA-SeMn-IR or extracellular solution followed by 43 h 6-OHDA (250 μ M) exposure. After different treatments, the open field swimming behavior of zebrafish on day 2 was assessed (Figure 7b), and their trajectories and velocities were captured by an automated tracking system within 1 h observation (Figure 7c and Video 5). 6-OHDA-lesioned zebrafish had impaired motor patterns, exhibiting the shortest locomotion distance, lowest velocity, and longest rest time (Figure 7d–f). mPDA-SeMn-IR alone and photothermal therapy remarkably restored motor function, outperforming NIR-II alone and matching the clinical benchmark Madopar (levodopa/benserazide combination therapy).

As aforementioned, TH reduction reflects nigrostriatal dopaminergic neurodegeneration. The TH-P2A-EGFP knock-in zebrafish (3-dpf) were used to assess midbrain TH-

positive (TH⁺) neurons (Figure 7g and Figure S29). 6-OHDA lesioning decreased the TH⁺ neuron area to 53.2% of controls, which was partially reversed by mPDA-SeMn-IR (68.8% recovery) but fully restored through photothermal activation or Madopar (Figure 7h,i). These results suggested that photothermal activation inhibited the degeneration of dopaminergic neurons from elevated brain dopamine levels. 8,63

CONCLUSIONS

Photoactive nanomaterials have wide applications in a physiological environment. Among those, emerging nongenetic Ca²⁺ photomodulation strategies employ diverse mechanisms, including photocatalytic IP₃R activation, phototriggered RyR S-nitrosylation, photothermal endogenous TRPV1 stimulation, photothermal lysosomal Ca²⁺ leakage, light-controlled liposomal agonist release, phototo-

acoustic mechanotransduction,⁷² light-driven molecular motors for IP₃ signaling,⁷³ and optoelectronic VGCC opening. 59,60 Compared to those strategies, our photothermal ER Ca²⁺ release method possesses four advantages: (1) spatiotemporal precision with subcellular targeting and millisecond latency via confocal photoexcitation (Figures 5a and 6a); (2) repeatable activation enabled by robust photothermal stability (Figure 21) and precise temperature control within cellular thermal tolerance thresholds (Figures 5b and 6b and Figures S21 and S27); (3) biological universality due to ubiquitous IP₃R expression; and (4) deep tissue penetration using 1064 nm lasers with low absorption/scattering. Our future goals include testing untethered photothermal stimulation in freely moving PD mice, building on pioneering work by Pu and Hong's team, who achieved deep dopaminergic neuron activation (6 mm beneath the scalp) with 71% photothermal efficiency (vs our 61% at 1064 nm). 14

Before rodent and primate studies can be advanced, it is imperative to evaluate the potential risks of overheating and Ca²⁺ overload. Photothermal heating (2 W/cm², 90 s) increased temperature within the physiological range (37.6 °C, Figure S30) and maintained >99% cell viability (Figure S31). Moreover, the sustained cytosolic Ca²⁺ concentration (lasting several hours) may induce mitochondrial dysfunction, oxidative stress, and apoptosis. 74-76 Our strategy of transient Ca²⁺ responses (minute-scale) with on-demand repetitive stimulation achieves (1) controlled neuromodulation, mimicking the physiological pulsatile Ca2+ dynamics; (2) mitigated cytotoxicity, preventing Ca2+ overload-induced neuronal damage; and (3) precision control, enabling spatiotemporal targeting of TH activation. Prolonged hyperthermia exposure (>43 °C for hours) dramatically inhibits mitochondrial respiratory complexes activity, thereby disrupting electron transport chain function and subsequently enhancing electron leakage with enhanced superoxide anion (O2 •-) generation. 77-79 Notably, repeated photothermal stimulation (9 cycles, 2 W/cm², 80 s/cycle) did not elevate intracellular ROS levels compared to the control (Figure S32). This outcome was attributed to two key factors: (1) tolerable thermal parameters. Moderate temperature elevation within the physiological range (37.6 °C, Figure S30) and short duration (80 s) prevented overheating; (2) mPDA-SeMn-IR's intrinsic antioxidant capacity could neutralize heat stress triggered oxidative stress (Figure 3). There was no increase in α -syn expression (Figure S33), mitochondrial membrane potential loss (Figure S34), or caspase-3/7 activity (Figure \$35) after photothermal treatment.

Ca²⁺-mediated neuroinflammatory responses represent a critical safety consideration. Photothermal stimulation elicited repeatable Ca²⁺ transients in murine BV-2 microglia (Figure S36a-c). Immunofluorescence staining revealed that 100 μ M H₂O₂-treated BV-2 cells significantly increased pro-inflammatory marker CD86 expression and were polarized into a deramified state. In contrast, both mPDA-SeMn-IR and mPDA-SeMn-IR + NIR groups exhibited CD86 levels comparable to the control without noticeable morphological change (Figure S36d). All groups showed similar expressions of the anti-inflammatory marker CD206 (Figure S36e). 100 μM H₂O₂-treated BV-2 cells secreted significantly more proinflammatory cytokine IL-6 than the mPDA-SeMn-IR and mPDA-SeMn-IR + NIR groups. All groups secreted comparable levels of anti-inflammatory IL-10 (Figure S36f,g). Collectively, photothermal Ca²⁺ modulation in BV-2 cells did

not drive pro-inflammatory polarization or cytokine release. While Ca²⁺ signaling participates in microglial activation, M1 polarization requires coordinated multifactorial stimuli beyond Ca²⁺ dynamics.

Zebrafish PD models have several advantages and have been widely used for drug screening and NP-based therapeutics (details are described in Section 8.2 in the Supporting Information (SI)). Compared to zebrafish PD models, mouse PD models better mimic human PD's pathology and symptoms. The primary challenge for mPDA-SeMn-IR application in mouse PD models lies in achieving sufficient blood-brain barrier (BBB) penetration and targeted accumulation. Effective nanotransducer-mediated neuromodulation requires localized enrichment at disease sites, yet the BBB intrinsically limits the passive transport. Although Kim's team used locally generated nitric oxide to transiently open BBB for efficient NP accumulation in subthalamic nucleus,8 most studies used stereotaxic injections to inject NPs to stratum, STN, ^{7,15,59} and substantia nigra (SN). ¹⁷ In our future work, we will rigorously evaluate mPDA-SeMn-IR's BBB traversal efficiency and implement optimized delivery strategies accordingly.

Overall, we developed mPDA-SeMn-IR, an implant-free nanoactuator integrating NIR-II photothermal activation and ROS-scavenging capabilities for innovative PD therapy. This system enabled noninvasive ER Ca2+ efflux-mediated DBS through IP₃R stimulation, which enhanced dopamine biosynthesis (elevated TH expression/activation) and release. Simultaneously, synergistic oxidative stress mitigation demonstrated exceptional neuroprotection against 6-OHDA-induced neurotoxicity, thereby preserving more neurons for photothermal activation. In vivo, photothermal activation could efficiently stimulate midbrain neurons and control the coiling behavior of embryonic zebrafish. In the zebrafish PD model, mPDA-SeMn-IR restored locomotor capacity and preserved the TH⁺ neurons. By combining wireless controllability with dual-modality therapy, our system provides an advanced therapeutic strategy for the treatment of neurodegenerative diseases.

METHODS

All experimental details are described in the Supporting Information. Due to the length of this article, only some experimental information is presented in the manuscript.

Preparation of Polydopamine (mPDA) NPs. mPDA NPs were prepared according to others' protocol.80 The chemical structure of the self-polymerization of dopamine in the presence of oxygen and ammonia is shown in Figure S1. Briefly, Pluronic F-127 (Sigma-Aldrich, #P2443, 1 g) and dopamine hydrochloride (Innochem, #A76711, 0.5 g) were dissolved in ethanol (50 mL) and water (50 mL). The mixture was allowed to stand at 30 °C for 30 min. Afterward, 1,3,5-trimethylbenzene (Energy Chemical, #W310156, 2 mL) was slowly added into the mixture under stirring (500 rpm). After further incubation for 60 min, an ammonia solution (Sinopharm, #18510157, 25-28 wt %, 5 mL) was added to the mixture at a rate of 0.5 mL/min by an auto syringe pump to create an alkaline condition. After stirring for 3 h, mPDA NPs were collected by centrifugating at 10,000 rpm for 10 min and washed by ultrapure water and ethanol trice, respectively. mPDA NPs were resuspended in water and stored at 4 °C before use.

Preparation of mPDA-SeMn. 2-(Penylselanyl)ethan-1-amine was conjugated onto mPDA NPs to obtain mPDA-Se NPs through the formation of Schiff base or via a Michael addition reaction (Figure S7). ** mPDA NPs (20 mg) were dispersed in 0.1 M NaHCO3 aqueous solution (2 mL) and sonicated for 1 min before adding SePh

(20 mg) in ethanol (0.4 mL). On the next day, mPDA-Se NPs were collected by centrifugation at 10,000 rpm for 10 min and washed by water trice.

PAH-MnO $_2$ NPs were absorbed on the mPDA-Se NPs via electrostatic interaction. mPDA-Se NP aqueous solution was slowly added into the PAH-MnO $_2$ NP aqueous solution at a mPDA-Se/PAH-MnO $_2$ weight ratio of 1/5 under vigorous stirring. The mixture was sonicated for 5 min and shaken for 10 min. Finally, the product was collected by centrifugation at 10,000 rpm for 10 min and washed with water thrice. mPDA-SeMn were resuspended in water and stored at 4 $^{\circ}$ C before use.

Preparation of mPDA-SeMn-IR. IR-1048-CONHS could react with the free amine group of the PAH-MnO $_2$ NPs. Briefly, mPDA-SeMn (5 mg) were dispersed in NaHCO $_3$ (0.1 M, 1 mL) aqueous solution. Then, freshly prepared IR-1048-CONHS (1 mg) in 3 mL of DMF was added quickly. The mixture was shaken overnight in the dark. Finally, the product was collected by centrifugation at 10,000 rpm for 10 min and washed with ethanol and water thrice. mPDA-SeMn-IR NPs were resuspended in water and stored at 4 $^{\circ}$ C before use.

SOD-Mimic Activity of mPDA and mPDA-SeMn-IR. The SOD-mimic activity of nanoenzymes was determined by the total superoxide dismutase assay kit with 2-[2-methoxy-4-nitrophenyl]-3-[4-nitrophenyl]-5-[2,4-disulfophenyl]-2H-tetrazolium (WST-8) (Biosharp, #BL903A). SOD-mimic can disproportionate superoxide radical (O2 •) into H2O2 and O2, with its activity inversely correlated with the residual $O_2^{\bullet-}$ concentration, as indicated by the conversion of WST-8 to deep-orange WST-formazan. The total volume of testing solutions was 200 μ L, and four groups were tested: (1) group 1—20 μ L of water, 160 μ L of WST-8 reaction solution, and 20 μ L of reaction start-up solution; (2) group 2—40 μL of water and 160 μL of WST-8 reaction solution; (3) group 3—20 μ L of water, 20 μ L of mPDA or mPDA-SeMn aqueous solution (25, 50, and 75 μ g/mL), 160 μ L of WST-8 reaction solution, and 20 μ L of reaction start-up solution; (4) group 4: 20 µL of mPDA or mPDA-SeMn-IR aqueous solution (25, 50, and 75 μ g/mL), 160 μ L of WST-8 reaction solution, and 20 μ L of reaction start-up solution. The reaction was incubated at 37 °C for 30 min. Afterward, the absorbance at 450 nm was measured with a microplate reader. The O2 •- elimination ratio was calculated according to the equation shown below.

elimination ratio =
$$\frac{(A_1 - A_2) - (A_4 - A_3)}{A_1 - A_2} \times 100\%$$
 (1)

 A_1 - A_4 : the absorbance of testing solutions in each corresponding group.

CAT-Like Mimic of mPDA and mPDA-SeMn-IR. The CAT-mimic activity was determined by a catalase assay kit (Beyotime, #S0051). mPDA and mPDA-SeMn-IR aqueous solution (600, 900, and 1200 μ g/mL) were incubated with 10 mM H_2O_2 aqueous solution at room temperature for 10 h, prior to the addition of the reaction stop solution. The above system was reacted with the chromogenic working solution at room temperature for 15 min and then detected by a microplate reader at 520 nm. The H_2O_2 elimination ratio was calculated according to the equation shown below.

elimination ratio =
$$\frac{c_1 - c_2}{c_1} \times 100\%$$
 (2)

 c_1 and c_2 are the initial and residual $\mathrm{H}_2\mathrm{O}_2$ concentrations, respectively.

***OH Scavenging Activity of mPDA and mPDA-SeMn-IR.** Salicylic acid (SA) can be converted to 2,3-dihydroxybenzoic acid after being oxidized by *OH, which can be scavenged by mPDA and mPDA-SeMn-IR. Therefore, the characteristic absorbance of 2,3-dihydroxybenzoic acid at 510 nm can be used as an indicator to measure the *OH scavenging activity. To generate *OH, equal volumes of 1.8 mM FeSO₄ and 5 mM H₂O₂ aqueous solution were mixed and allowed to react for 10 min. The total volume of testing solutions was 1.5 mL, and three groups were tested: (1) group 1—

500 μ L of water and 1 mL of *OH-containing solution; (2) group 2—1.5 mL of water; (3) group 3—500 μ L of mPDA, or mPDA-SeMn-IR aqueous solution (75, 150, and 300 μ g/mL) and 1 mL of *OH-containing solution. The testing solutions were incubated at room temperature for 30 min. Afterward, the mixture was centrifuged at 10,000 rpm for 6 min, and the supernatant (600 μ L) was added into the SA (Macklin, #S817529—250 g, 8 mM, 200 μ L) aqueous solution. After reaction for 2 min, the absorbance of 2,3-dihydroxybenzoic at 510 nm was measured using a microplate reader. The elimination ratio of *OH was calculated according to eq 3.

elimination ratio =
$$\frac{(A_1 - A_2) - (A_3 - A_2)}{A_1 - A_2} \times 100\%$$
 (3)

 A_1 - A_3 : absorbance of testing solutions in each corresponding group.

 H_2O_2 Concentration-Dependent Degradation of mPDA-SeMn. To measure mPDA-SeMn degradation in H_2O_2 solution, 0.02 mL of H_2O_2 aqueous solution was added into 1.98 mL of 150 μ g/mL mPDA-SeMn aqueous solution to make final H_2O_2 concentrations at 0, 0.5, 2, and 8 mM. The solution was incubated at 37 °C. Every 12 h, the absorbance was measured and an additional 0.02 mL of H_2O_2 aqueous solution was supplemented. After 84 h, the morphology and size of mPDA-SeMn were measured by TEM.

mPDA-, mPDA-Se-, and mPDA-SeMn-IR-Induced Cytotoxicity. 2×10^4 PC-12 cells in 100 μ L of cell culture medium were seeded into each well of 96-well plates (seeding area: $0.32~\rm cm^2$) and incubated for 2 days. On the third day, the old medium was removed, and cells were incubated with different concentrations (0, 0.5,1, 2, 4, 8, 16, 32, 64, and 128 μ g/mL) of NPs in 100 μ L of serum-free culture medium for 24 h. Cells not exposed to NPs were used as the positive control (i.e., 100% cell viability). According to the manufacturer's manuals (https://www.sigmaaldrich.com/deepweb/assets/sigmaaldrich/product/documents/129/020/96992-product-information.pdf), mPDA, mPDA-Se, and mPDA-SeMn-IR with reducing activity may react with WST-8 to give a false reading. This has also been mentioned by reviewers of our previous publication. Therefore, cytotoxicity was determined by the methylene blue assay for cells, 33 which was based on the number of living cells.

The staining solution was prepared by adding methylene blue (Energy Chemical, #E0214780250, final concentration: 0.6 wt %) and glutaraldehyde solution (final concentration: 1.25 wt %) into Hank's balanced salt solution (HBSS, Biosharp, #BL561A). The old medium was removed, and cells in each well were incubated with 50 μL of staining solution at 37 °C for 60 min. Then, the staining solution was removed, and cells were gently rinsed with distilled water eight times. The excess water was removed, and the plate was air-dried for 60 min. Elution solution (50% ethanol + 49% PBS + 1% acetic acid, 100 μL) was added to each well. Finally, 90 μL of the supernatant was taken out, and its absorbance at 662 nm was measured with a microplate reader.

BioTEM Imaging of PC-12 Cells Treated with mPDA-SeMn-IR and 6-OHDA. To observe intracellular mPDA-SeMn-IR distributions and the morphology change of mitochondria, we performed TEM imaging. 4×10^5 PC-12 cells in 2 mL of cell culture medium were seeded into each well of six-well plates (seeding area: 9.6 cm²) and incubated for 2 days. Four groups of cells were used for TEM imaging: (1) control group without treatment; (2) cells treated with 6-OHDA (100 μ M) in serum-free culture medium for 12 h; (3) cells treated with mPDA-SeMn-IR (10 μ g/mL) in serum-free culture medium for 12 h; (4) cells cotreated with mPDA-SeMn-IR (10 µg/ mL) and 6-OHDA (100 μ M) in serum-free culture medium for 12 h. Cells from five wells in the same groups were collected in the 2 mL centrifuge tube, fixed with 2.5% glutaraldehyde in PBS at 4 °C overnight. Afterward, cells were further fixed by 1% osmium acid solution for 1-2 h, dehydrated, embedding in the resin, ultra sectioned (70-90 nm), and stained by reduced osmium-thiocarbohydrazide-osmium (rOTO) solution. These steps were accomplished by the Analysis Center of Agrobiology and Environmental Sciences in

Zhejiang University. Finally, cells were imaged by Hitachi HT7820 TEM.

To measure mPDA-SeMn degradation in 6-OHDA-treated PC-12 cells, 4 \times 10^{5} PC-12 cells in 1.5 mL of cell culture medium were seeded into each well of six-well plates (seeding area: 9.6 cm²) and incubated for 2 days. Cells were incubated mPDA-SeMn (10 $\mu g/\text{mL}$) and 6-OHDA (100 μM) in serum-free culture medium for 12 h. Cells were then subjected to cyclic oxidative challenges comprising sequential 12 h incubations: the medium was replaced with fresh cell culture medium for 12 h, followed by 12 h treatment with 6-OHDA (100 μM) in serum-free culture medium. This step was repeated two times, and cells were recovered in fresh complete medium for 12 h. Finally, cells from five wells in the same groups were collected in the 2 mL EP tube for BioTEM imaging.

mPDA-SeMn-IR-Protected Cells from 6-OHDA-Induced Cell Death. 6×10^4 PC-12 cells (6×10^4) in 300 μ L of cell culture medium was seeded in each well of an eight-well chambered cover glass (Cellvis, #C8-1.5H-N, seeding area: 0.81 cm²) and incubated for 2 days. On the third day, cells were divided into four groups: (1) control group without treatment; (2) cells were incubated with mPDA-SeMn in serum-free culture medium (10 μ g/mL, 200 μ L) for 12 h; (3) cells were incubated with 6-OHDA (100 μ M, 200 μ L) in serum-free culture medium for 12 h; and (4) cells were incubated with 6-OHDA (100 μ M) and NP (10 μ g/mL) in serum-free culture medium (200 μ L) for 12 h.

Two staining solutions were prepared for live/dead staining. To stain live cells, fluorescein diacetate (FDA, Aladdin, #F109384-1g) was dissolved in anhydrous DMSO to obtain a freshly prepared stock solution (2 mM). When nonfluorescent FDA molecules enter living cells, they are digested by the esterase to yield highly fluorescent fluorescein. To stain the dead cells, propidium iodide (PI, Energy Chemical, #BR0005-50 mg) was dissolved in water to obtain a 4 mM stock solution. This solution can be stored at $-20\,^{\circ}\mathrm{C}$ for 3 months. PI can only enter cells with damaged cell membranes, and therefore, it only labels dead cells. The working solution was prepared by adding 2 $\mu\mathrm{L}$ of FDA (2 mM) and 1 $\mu\mathrm{L}$ of PI (4 mM) to 1 mL of HBSS. Note that the working solution should be used immediately. Cells in each well were incubated with 200 $\mu\mathrm{L}$ of working solution at 37 °C for 15 min. Afterward, cells were washed with HBSS trice.

Effects of Different Formulations on Intracellular ROS Level and GSH/GSSG Ratios. Effects of MnO₂, mPDA, mPDA-Se, mPDA-Mn, and mPDA-SeMn-IR on intracellular ROS levels were investigated. 6×10^4 PC-12 cells in 300 μ L of cell culture medium were seeded in an eight-well chambered cover glass (seeding area: 0.81 cm²) and incubated for 2 days. On the third day, cells were divided into eight groups: (1) control group without treatment; (2) cells were incubated with MnO_2 (2.5 $\mu g/mL$) in serum-free culture medium (200 μ L) for 12 h; (3) cells were incubated with MnO₂ (10 $\mu g/mL$) in serum-free culture medium (200 μL) for 12 h; (4) cells were incubated with 6-OHDA (100 μ M, 200 μ L) in serum-free culture medium for 12 h; (5) cells were incubated with 6-OHDA (100 μ M) and mPDA (10 μ g/mL) in serum-free culture medium (200 μ L) for 12 h; (6) cells were incubated with 6-OHDA (100 μ M) and mPDA-Se (10 μ g/mL) in serum-free culture medium (200 μ L) for 12 h; (7) cells were incubated with 6-OHDA (100 μ M) and mPDA-Mn (10 $\mu g/mL$) in serum-free culture medium (200 μL) for 12 h; (8) cells were incubated with 6-OHDA (100 µM) and mPDA-SeMn-IR (10 μ g/mL) in serum-free culture medium (200 μ L) for 12 h. Afterward, cells were stained with H2DCFDA and observed by a confocal microscope.

Rosup, a ROS-positive inducer, ³⁹ was also applied to induce ROS increase in PC-12 cells. Cells are divided into four groups: (1) control group without treatment; (2) cells were incubated with mPDA-SeMn-IR in serum-free culture medium (10 μ g/mL, 200 μ L) for 24 h; (3) cells were incubated with diluted Rosup (50 μ g/mL, 200 μ L) in PBS for 20 min; (4) cells were incubated with mPDA-SeMn-IR in serum-free culture medium (10 μ g/mL, 200 μ L) for 24 h, followed by incubation with diluted Rosup (50 μ g/mL, 200 μ L) in PBS for 20 min

To visualize the intracellular ROS levels, cells were incubated with freshly prepared 2',7'-dichlorodihydrofluorescein diacetate (H2DCFDA, 10 μM , 200 μL , Beyotime, #S0033S) in HBSS for 30 min. To stain the nuclei, cells were stained with Hoechst 33342 (10 $\mu\text{g}/\text{mL}$, 200 μL) in HBSS for 10 min. Afterward, cells were washed with HBSS trice.

Effects of MnO₂, mPDA, mPDA-Se, mPDA-Mn, and mPDA-SeMn-IR on GSH/GSSG were investigated. 4×10^5 PC-12 cells in 2 mL of cell culture medium were seeded in a six-well plate (seeding area: $9.5~\rm cm^2$) and incubated for 2 days. On the third day, cells were divided into eight groups as aforementioned. Afterward, cells were washed with PBS twice and collected by gentle pipetting. The GSH and GSSG concentrations were detected by a GSH and GSSG Assay Kit (Beyotime, #S0053). We note that the GSH/GSSG ratio is a more reliable indicator of cellular redox status than absolute GSH content as it avoids artifacts from incomplete cell collection or cell death-induced GSH depletion.

Activation of Caspase-3/7 Activity. 6×10^4 PC-12 cells in 300 μL of cell culture medium were seeded in an eight-well chambered cover glass (seeding area: 0.81 cm²) and incubated for 2 days. On the third day, cells are divided into seven groups: (1) control group without treatment; (2) cells were incubated with mPDA-SeMn-IR in serum-free culture medium (10 μ g/mL, 200 μ L) for 12 h; (3) cells were incubated with 6-OHDA (100 μ M, 200 μ L) in serum-free culture medium for 12 h; (4) cells were incubated with 6-OHDA (100 μ M) and mPDA-SeMn-IR (10 μ g/mL) in serum-free culture medium (200 μ L) for 12 h; (5) cells were incubated with ionomycin in serum-free culture medium (1 μ M, 200 μ L) for 12 h; (6) cells were irradiated with 1064 nm laser (2 W/cm², 1 min); (7) cells were incubated with mPDA-SeMn-IR in serum-free culture medium (10 μ g/mL, 200 μ L) for 12 h and then irradiated with 1064 nm laser (2 W/cm², 1 min). Cells were illuminated nine times, three in the morning, three in the afternoon, and three in the evening, with a 30 min interval.

The caspase-3/7 activity in live cells was detected by the GreenNuc Caspase-3 Assay Kit for Live Cells (Beyotime, #C1168S). The rationale is that the DEVD peptide in the GreenNuc caspase-3/7 substrate can be specifically cleaved by caspase-3, and the released fluorophore can be detected. Cells were incubated with GreenNuc caspase-3 substrate in HBSS (200 μ L, 5 μ M) for 20 min at room temperature. To stain the nucleus, cells were incubated with Hoechst 33342 (200 μ L, 10 μ g/mL) in HBSS at 37 °C for 10 min and washed with HBSS trice.

The Protocol for Photoexcitation and Imaging. We have applied two photoexcitation strategies, i.e., single-cell irradiation and whole-plate irradiation, to activate the cell Ca²⁺ response. To real-time monitor the change of Fluo-8 fluorescence, we utilized a confocal 488 nm laser at a laser power lower than $P_{\rm laser}=16.1~\mu{\rm W}$ (i.e., <0.7% of maximum laser power), which was incapable of generating sufficient photothermal heating. The scanning duration per frame was less than 0.9 s, and 106 frames were taken.

For single-cell irradiation, a custom-made region in one cell containing a single particle or several aggregated particles was photoexcited by the 488 nm laser in CLSM900. Briefly, the "Experiment Regions" and "Bleaching" modules in ZEN 3.3 blue edition software were utilized. As described in our previous publication, the frequently used irradiation time $\Delta t_{\rm laser}$ was 0.16 s, and a typical irradiation area $A_{\rm laser}$ was 15.2 $\mu{\rm m}^2$. Both parameters can be directly read from ZEN 3.3 blue edition software in the "Graphics" and "Graphics" modules. Note that both $\Delta t_{\rm laser}$ and $A_{\rm laser}$ varied from case to case. The maximum laser power at 488 nm was used for photoexcitation. mPDA-SeMn were irradiated only in the custom-made regions at the desired time. To repeatedly photoexcite cells, different regions containing mPDA-SeMn were irradiated with an interval of 120 s. As the duration of photoexcitation was short, it could be roughly assumed that photoexcitation and imaging happened simultaneously.

For whole plate irradiation, an external 1064 nm laser pointer (China Ningbo Fingco Optoelectronic Co., Ltd.) was used to photoexcite all cells. Two zoom fiber collimators were custom-

designed and coupled with the laser pointer, with a laser spot diameter of 1 or 2.5 cm. This appropriate laser spot was chosen according to the well area of different plates. During laser irradiation, the cells were continuously imaged. The position of the laser spot was visualized with a viewing card. We also integrated a laser beam homogenizer to transform the input laser beam into a more uniform intensity distribution. The output laser power density was 2 W/cm². To repeatedly photoexcite cells, cells were irradiated with a 1064 nm laser (2 W/cm², 80 s) with an interval of 10 min. To simultaneously visualize cytosolic Ca2+ and photoexcite NPs, PC-12 cells were incubated with mPDA-SeMn-Cy5 (3 µg/mL) and mPDA-SeMn-IR $(7 \mu g/mL)$ in serum-free culture medium for 24 h. Of note, additional mPDA-SeMn-IR NPs (200 μ g/mL) were added into cells just before irradiation to improve Ca²⁺ activation efficiency by the 1064 nm laser. Afterward, NPs were removed. The data were analyzed by MATLAB2019a. Fluorescence was normalized to the average value calculated from the data prior to irradiation.

Immunostaining Analysis of Ca2+-Enhanced Expression of **TH.** 6×10^4 PC-12 cells (6×10^4) in 300 μ L of cell culture were seeded in an eight-well chambered cover glass (seeding area: 0.81 cm²) and incubated for 2 days. The whole plate irradiation was applied in this experiment. Details about whole-plate irradiation can be found in Section 7.2 the protocol for photoexcitation and imaging. On the third day, cells were divided into seven groups—on the next day, cells were divided into seven groups: (1) control group without treatment; (2) cells were incubated with mPDA-SeMn in serum-free culture medium (10 µg/mL, 200 µL) for 12 h; (3) cells were incubated with 6-OHDA (100 μ M, 200 μ L) in serum-free culture medium for 12 h; (4) cells were incubated with 6-OHDA (100 μ M) and mPDA-SeMn (10 μ g/mL) in serum-free culture medium (200 μ L) for 12 h; (5) cells were incubated with ionomycin in serum-free culture medium (1 µM, 200 µL) for 12 h; (6) cells were irradiated with 1064 nm laser (2 W/cm², 1 min); (7) cells were incubated with mPDA-SeMn-IR in serum-free culture medium (10 μ g/mL, 200 μ L) for 12 h, with additional mPDA-SeMn-IR (200 $\mu g/mL$, 100 μL), and irradiated with 1064 nm laser (2 W/cm², 1 min). Cells were illuminated nine times, three in the morning, three in the afternoon, and three in the evening, with a 30 min interval. TH expression was detected by immunofluorescence staining. The primary antibody was rabbit TH polyclonal antibody (Elabscience, #E-AB-70077), and the dilution time was 150×.

Dopamine Biosynthesis from PC-12 Cells Quantified by an **ELISA Kit.** 4×10^5 PC-12 cells in 1 mL of cell culture medium were seeded in a six-well plate (seeding area: 9.5 cm²) and incubated for 2 days. On the third day, cells were divided into four groups: (1) G1 control group without treatment; (2) G2—cells were incubated with mPDA-SeMn in serum-free culture medium (10 μ g/mL, 1 mL) for 12 h; (3) G3—cells were first incubated with mPDA-SeMn-IR in serumfree culture medium (10 μ g/mL, 1 m) for 12 h and irradiated with 1064 nm laser (2 W/cm², 1 min). Cells were illuminated nine times, three in the morning, three in the afternoon, and three in the evening, with a 30 min interval. After photothermal activation, cells were further incubated for 12 h. (4) G4: cells were incubated with ionomycin in cell culture medium (1 μ M, 1 mL) for 12 h. Cells were gently pipetted to be detached and transferred to a 1.5 mL EP tube. A hand-held tip sonicator was employed to rupture the cell samples under ice bath. The mixture was centrifuged at 1000g for 3 min. The supernatant was diluted three times, and total dopamine amount was detected using an ELISA kit (Elabscience, #E-EL-0046).

Dopamine Release from PC-12 Cells Visualized by a Fluorescent False Neurotransmitter. Voltage-gated Ca²⁺ channels also regulate the exocytotic release of dopamine: Ca²⁺ enters cells through these channels upon depolarization of neurons, which triggers dopamine-containing vesicle fusion with the presynaptic plasma membrane via the Ca²⁺ sensors synaptotagmin, thereby releasing dopamine.⁸⁺ Dopamine release cannot be directly observed by CLSM. The rationale is that vesicular monoamine transporter 2 transports FFNS11 from the cytoplasm into synaptic vesicles that contain dopamine; FFNS11 is released along with dopamine during

exocytosis, and the fluorescence in synaptic vesicles diminishes, rendering dopamine release observable. 54

 6×10^4 PC-12 cells in 300 μL of cell culture medium were seeded in an eight-well chambered cover glass (seeding area: $0.81~{\rm cm}^2)$ and incubated for 2 days. On the third day, the medium was removed, and 200 μL of mPDA-SeMn (10 $\mu g/mL$) in a cell culture medium was added. To visualize the cells, cells were incubated with freshly prepared FDA in HBSS (4 μM , 200 μL) at 37 °C for 15 min. FFNS11 (Aladdin, no. F274714) was dissolved in DMSO to prepare the stock solution (2 mM). Afterward, cells were incubated with FFNS11 (5 μM , 200 μL) in HBSS at 37 °C for 5 min. Cells were washed with HBSS three times before imaging. To visualize the [Ca²+] cyto change, FDA staining was replaced with Fluo-8 AM. The whole-plate irradiation was applied in this experiment. Cells were imaged during laser irradiation.

Animals. AB wild-type zebrafish (Danio rerio) at 0-10 dpf (days post fertilization) were purchased from Hangzhou Huante Biotechnology Co., Ltd. Zebrafish were kept in a zebrafish recirculating aquaculture system cultured at 28 \pm 0.5 °C with a 14 h light:10 h dark cycle. The medium was prepared by adding 200 mg of instant sea salt to 1 L of water. Conductivity, pH, and hardness were maintained at 450-550 μ S/cm, 6.5-8.5, and 50-100 mg/L CaCO₃, respectively, according to the Zebrafish International Resource Center guidelines.⁸⁵ The license number for the use of experimental animals is SYXK (Zhejiang) 2022-0004. The feeding management meets the requirements of the international AAALAC certification (certification number: 001458) and IACUC ethical certification (review number: IACUC-2023-6624-01). After experiments, euthanasia was carried out by incubating zebrafish with 1 wt % of 3-aminobenzoc acid ethyl ester methanesulfonate (MS-222, #E10505, Sigma-Aldrich) in water until cessation of heartbeat.

In Vivo Electrophysiological Recordings of Photoexcited Brain Neurons. All recordings were performed under ambient conditions according to previously published protocol. AB zebrafish at 10 dpf were anesthetized with 0.02 wt % MS-222 in water for approximately 1–2 min or until loss of reflex responses. The device was shown in the manuscript Figure 6d. About 5 nL of mPDA-SeMn-IR (2.5 mg/mL,12.5 ng) aqueous solution or water was injected directly into the ventricular space. The injection procedure was described in Section 8.4 distribution of mPDA-SeMn-Cy5 in zebrafish at 4 dpf. Subsequently, zebrafish were embedded in 1.5 wt % agarose with a low melting point. Note that we did not measure a single neuron in this case; rather, all the neurons in contact with the patch pipet were measured.

An external 1064 nm laser with a 1 cm laser spot diameter was coupled to an electrophysiology system for the local field voltage/ current recording of the electrophysiology of light-stimulated brain neurons. The brain was first measured without the laser for ca. 100 s to evaluate spontaneous neuronal excitability. Then, the brain was exposed to three cycles of laser irradiation (2 W/cm², 20 s) and laser off (30-40 s). The currents and voltages were recorded by holding the membrane potential at -60 mV using a K+-based intracellular solution (in mM: 110 potassium gluconate (Sigma-Aldrich, #G4500), 8 KCl, 5 NaCl, 1.5 MgCl₂, 20 HEPES, 0.5 ethylene glycol-bis(βaminoethyl ether)-N,N,N',N'-tetraacetic acid (EGTA, Sigma #324626, Aldrich), 2 ATP, and 0.3 GTP). Recording micropipettes were pulled from borosilicate glass capillaries (Warner Instruments, Hamden) with resistances of 400-500 k Ω when filled with a K⁺based intracellular solution. Liquid junction potential was adjusted during the recording process. The analysis utilized cells where the series resistance did not vary by more than 10%, and the input resistance (0.7–2 G Ω) remained relatively constant. Signals were collected every 1 ms and filtered at 2 kHz with a MultiClamp 700A amplifier (Molecular Devices, Palo Alto) and a Digidata 1440A data acquisition system.

Behavioral Test in the Zebrafish PD Model. The establishment of the zebrafish PD model was assisted by Hangzhou Huante Biotechnology Co., Ltd. The illustration of workflow is shown in Figure 7b. AB zebrafish at 4 dpf were randomly divided into six groups (N = 12 for each group): (1) control group without treatment;

(2) zebrafish were incubated with 3 mL of 6-OHDA (250 μ M) in the working solution for 43 h; (3) zebrafish were first intraventricularly injected with mPDA-SeMn-IR NPs (2.5 mg/mL, 5 nL, 12.5 ng) and then incubated with 3 mL of 6-OHDA (250 μ M) in the working solution for 43 h; (4) zebrafish were incubated with 3 mL of 6-OHDA (250 μ M) in the working solution for 43 h and irradiated with the 1064 nm laser (2 W/cm², 45 s, four times); (5) zebrafish were first intraventricularly injected with mPDA-SeMn-IR NPs (2.5 mg/mL, 5 nL, 12.5 ng), incubated with 3 mL of 6-OHDA (250 μ M) in the working solution for 43 h, and irradiated with the 1064 nm laser (2 W/cm², 45 s, four times); (6) zebrafish were incubated with 3 mL of working solution containing 6-OHDA (250 μM) and Madopar (Roche, #SH5822, 100 μ g/mL) for 43 h. Madopar is a clinically approved medicine for the treatment of Parkinson's disease, which contains levodopa and the decarboxylase inhibitor benserazide in the mass ratio of 4:1. Details regarding Madopar can be found the online document: https://assets.roche.com/f/170883/x/c3ff8d80bd/ madopar-pi jun-2023.pdf. Levodopa is converted to dopamine, and benserazide prevents levodopa from changing to dopamine in the bloodstream. Laser irradiation was conducted once on day 0 and three times on day 1.

On the third day, zebrafish were gently transferred to each well of the 96-well plates. The swimming behavior within 1 h was recorded by a camera and analyzed by behavior monitoring software (ZebraLab v3.22.3.31, ViewPoint). The swimming speeds were classified as fast (>20 mm/s), medium (4-20 mm/s), and slow (<4 mm/s).

Protection of TH+ Neurons in the Zebrafish PD Model. For zebrafish injected with mPDA-SeMn-IR NPs, 5 nL of mPDA-SeMn-IR NPs (2.5 mg/mL, 12.5 ng), TH-P2A-EGFP plasmid (Addgene, #65562), and Cas9 protein was coinjected into 0 dpf zebrafish at the 1-2 cell stages, conducted by the technician from Hangzhou Huante Biotechnology Co., Ltd. In this way, TH-P2A-EGFP knock-in zebrafish was established, which expressed both enhanced green fluorescent protein (GFP) and TH-P2A fusion protein. Therefore, EGFP serves as a colocalized indication with TH⁺-neuron. 86 On the next day, 1 dpf zebrafish were randomly divided into six groups (n = 8for each group): (1) control group without NP injection and other treatment; (2) zebrafish without NP injection were incubated with 3 mL of 6-OHDA (500 μ M) in the working solution for 48 h; (3) zebrafish injected with NPs were incubated with 3 mL of 6-OHDA (500 μ M) in the working solution for 48 h; (4) zebrafish were incubated with 3 mL of 6-OHDA (500 μ M) in the working solution for 48 h and irradiated with the 1064 nm laser (2 W/cm², 45 s, 7 times); (5) zebrafish injected with NPs were incubated with 3 mL of 6-OHDA (500 μ M) in the working solution for 48 h and irradiated with the 1064 nm laser (2 W/cm², 45 s, seven times); (6) zebrafish were incubated with 3 mL of working solution containing 6-OHDA (500 μ M) and Madopar (Roche, #SH5822, 100 μ g/mL) for 48 h. Laser irradiation was conducted once on day 0 and three times on days 1 and 2. Zebrafish were incubated with 0.02 wt % MS-222 in water for 1-2 min or until loss of reflex responses. The heads of zebrafish were imaged with a fluorescent microscope (AXIO Zoom.V16, ZEISS).

Statistical Analysis. Comparisons between experimental groups were made using one-way ANOVA without normality assumption, given its reasonable tolerance of violations to normal distribution. The experimental groups include cell viability (Figure 4f), intracellular ROS level (Figure 4i-2), α -syn expression (Figure 4j-2), JC-1 greento-red ratio (Figure 4k-2), AUC and maximum I_t/I_0 of Ca²⁺ fluorescence (Figure 5e), TH expression (Figure 5f-2), pTH expression (Figure 5g-2), dopamine concentration in the supernatant (Figure 5k), coiling behavior trial (Figure 6i), swimming distance (Figure 7d), average velocity (Figure 7e), rest time (Figure 7f), and area of TH⁺ neurons (Figure 7i). Comparisons between coiling behavior trials within 3 cycles of laser irradiation (Figure 6j) were made using one-tailed paired sample t test. No adjustments were made for multiple comparisons.

ASSOCIATED CONTENT

Supporting Information

The Supporting Information is available free of charge at https://pubs.acs.org/doi/10.1021/acsnano.5c06227.

All experiment details about materials synthesis and characterizations, in vitro and in vivo performance, and supporting figures and tables (PDF)

Single-cell Ca2+ dynamics in a PC-12 cell upon photoexcitation by localized confocal laser (MP4)

Repetitive stimulation of multiple PC-12 cells using a continuous-wave 1064 nm laser pointer (AVI)

Real-time monitoring of dopamine release from cells as indicated by decreased I(FFN551) in G5 and G7 (AVI)

Snap photos of coiling movement of an embryonic zebrafish during the 1064 nm laser irradiation (MP4)

Trajectories and speed of PD zebrafish model after different treatment within 2 min of observation (MP4)

AUTHOR INFORMATION

Corresponding Authors

Baiheng Wu – Key Laboratory of Organosilicon Chemistry and Material Technology, Ministry of Education, Zhejiang Key Laboratory of Organosilicon Material Technology, College of Material, Chemistry and Chemical Engineering, Hangzhou Normal University, Hangzhou, Zhejiang 311121, China; orcid.org/0000-0003-3753-5407; Email: bhwu@hznu.edu.cn

Junqiu Liu – Key Laboratory of Organosilicon Chemistry and Material Technology, Ministry of Education, Zhejiang Key Laboratory of Organosilicon Material Technology, College of Material, Chemistry and Chemical Engineering, Hangzhou Normal University, Hangzhou, Zhejiang 311121, China; orcid.org/0000-0003-1608-7908; Email: junqiuliu@ hznu.edu.cn

Dingcheng Zhu – *Key Laboratory of Organosilicon Chemistry* and Material Technology, Ministry of Education, Zhejiang Key Laboratory of Organosilicon Material Technology, College of Material, Chemistry and Chemical Engineering, Hangzhou Normal University, Hangzhou, Zhejiang 311121, China; orcid.org/0000-0002-5636-4976; Email: zhudc@hznu.edu.cn

Authors

Chen Zhou – Key Laboratory of Organosilicon Chemistry and Material Technology, Ministry of Education, Zhejiang Key Laboratory of Organosilicon Material Technology, College of Material, Chemistry and Chemical Engineering, Hangzhou Normal University, Hangzhou, Zhejiang 311121, China

Feifei Wu - Key Laboratory of Organosilicon Chemistry and Material Technology, Ministry of Education, Zhejiang Key Laboratory of Organosilicon Material Technology, College of Material, Chemistry and Chemical Engineering, Hangzhou Normal University, Hangzhou, Zhejiang 311121, China

Liqing He – Key Laboratory of Organosilicon Chemistry and Material Technology, Ministry of Education, Zhejiang Key Laboratory of Organosilicon Material Technology, College of Material, Chemistry and Chemical Engineering, Hangzhou Normal University, Hangzhou, Zhejiang 311121, China

Huijie Yan - Key Laboratory of Organosilicon Chemistry and Material Technology, Ministry of Education, Zhejiang Key Laboratory of Organosilicon Material Technology, College of

- Material, Chemistry and Chemical Engineering, Hangzhou Normal University, Hangzhou, Zhejiang 311121, China
- **Zhaowei Zhang** Department of Orthopaedic Surgery, Sir Run Run Shaw Hospital, Zhejiang University School of Medicine, Hangzhou, Zhejiang 310016, China
- Shuang Zhao Key Laboratory for Special Fiber and Fiber Sensor of Hebei Province, School of Information Science and Engineering, Yanshan University, Qinhuangdao 066004, China
- Wenyi Huang Zhejiang Key Laboratory of Organ Development and Regeneration, College of Life and Environmental Sciences, Hangzhou Normal University, Hangzhou, Zhejiang 310036, China
- Yuhao Luo Zhejiang Key Laboratory of Organ Development and Regeneration, College of Life and Environmental Sciences, Hangzhou Normal University, Hangzhou, Zhejiang 310036, China; orcid.org/0000-0002-9392-5760
- Wei Zhao Key Laboratory of Organosilicon Chemistry and Material Technology, Ministry of Education, Zhejiang Key Laboratory of Organosilicon Material Technology, College of Material, Chemistry and Chemical Engineering, Hangzhou Normal University, Hangzhou, Zhejiang 311121, China
- Bulong Gao Key Laboratory of Organosilicon Chemistry and Material Technology, Ministry of Education, Zhejiang Key Laboratory of Organosilicon Material Technology, College of Material, Chemistry and Chemical Engineering, Hangzhou Normal University, Hangzhou, Zhejiang 311121, China
- Zherui Zhang Key Laboratory of Organosilicon Chemistry and Material Technology, Ministry of Education, Zhejiang Key Laboratory of Organosilicon Material Technology, College of Material, Chemistry and Chemical Engineering, Hangzhou Normal University, Hangzhou, Zhejiang 311121, China
- Yaofeng Zhou Westlake University, Hangzhou, Zhejiang 310024, China

Complete contact information is available at: https://pubs.acs.org/10.1021/acsnano.5c06227

Author Contributions

[†]C.Z. and F.W. contributed equally to this work.

Author Contributions

D.Z., B.W., and J.L. conceived the idea, designed the study, and directed the project. C.Z. performed most experiments and analyzed the data. F.W., L.H., and H.Y. assisted with zebrafish experiments. S.Z. assisted with dopamine concentration measurement. W.H. and Y.L. assisted with electrophysiological recordings. W.Z., B.G., and B.W. assisted with NP preparation. Zhaowei Z. assisted with transcriptome sequencing analysis. Zherui Z. provided insightful advice. D.Z. wrote the manuscript with help from all the authors.

Notes

The authors declare no competing financial interest.

ACKNOWLEDGMENTS

Chen Zhou and Feifei Wu contributed equally to this work. This work was supported by the National Natural Science Foundation of China (No. 22475059), Hangzhou Leading Innovation and Entrepreneurship Team Project (TD2022001), Interdisciplinary Research Project of Hangzhou Normal University (2024JCXK01), S&T Program of Hebei (236Z1705G), and Science and Technology Project of Hebei

Education Department (BJ2025057). We are grateful for the BioTEM support by the Analysis Center for Agrobiology and Environmental Sciences in Zhejiang University.

REFERENCES

- (1) Morris, H. R.; Spillantini, M. G.; Sue, C. M.; Williams-Gray, C. H. The Pathogenesis of Parkinson's Disease. *Lancet* **2024**, 403, 293–304.
- (2) Charvin, D.; Medori, R.; Hauser, R. A.; Rascol, O. Therapeutic Strategies for Parkinson Disease: Beyond Dopaminergic Drugs. *Nat. Rev. Drug. Discovery* **2018**, *17*, 804–822.
- (3) deSouza, R. M.; Moro, E.; Lang, A. E.; Schapira, A. H. Timing of Deep Brain Stimulation in Parkinson Disease: A Need for Reappraisal? *Ann. Neurol.* **2013**, *73*, 565–575.
- (4) Zhao, D.; Feng, P. J.; Liu, J. H.; Dong, M.; Shen, X. Q.; Chen, Y. X.; Shen, Q. D. Electromagnetized-Nanoparticle-Modulated Neural Plasticity and Recovery of Degenerative Dopaminergic Neurons in the Mid-Brain. *Adv. Mater.* **2020**, *32*, No. 2003800.
- (5) Chen, Y.-X.; Feng, P.-J.; Zhong, G.; Liu, J.-H.; Jiang, B.; Harn, Y.-W.; Zhao, D.; Lin, Z.; Zhang, Q.; Shen, Q.-D. Piezoelectric Nanogenerators Enabled Neuromodulation Rescued Dopaminergic Neuron Loss in Parkinson's Disease. *Nat. Energy* **2024**, *121*, No. 109187.
- (6) Yuan, J.; Liu, H.; Zhang, H.; Wang, T.; Zheng, Q.; Li, Z. Controlled Activation of Trpv1 Channels on Microglia to Boost Their Autophagy for Clearance of Alpha-Synuclein and Enhance Therapy of Parkinson's Disease. *Adv. Mater.* **2022**, *34*, No. 2108435.
- (7) Hescham, S. A.; Chiang, P. H.; Gregurec, D.; Moon, J.; Christiansen, M. G.; Jahanshahi, A.; Liu, H.; Rosenfeld, D.; Pralle, A.; Anikeeva, P.; Temel, Y. Magnetothermal Nanoparticle Technology Alleviates Parkinsonian-Like Symptoms in Mice. *Nat. Commun.* **2021**, *12*, 5569.
- (8) Kim, T.; Kim, H. J.; Choi, W.; Lee, Y. M.; Pyo, J. H.; Lee, J.; Kim, J.; Kim, J.; Kim, J. H.; Kim, C.; Kim, W. J. Deep Brain Stimulation by Blood—Brain-Barrier-Crossing Piezoelectric Nanoparticles Generating Current and Nitric Oxide under Focused Ultrasound. *Nat. Biomed. Eng.* 2023, 7, 149—163.
- (9) Oehrn, C. R.; Cernera, S.; Hammer, L. H.; Shcherbakova, M.; Yao, J.; Hahn, A.; Wang, S.; Ostrem, J. L.; Little, S.; Starr, P. A. Chronic Adaptive Deep Brain Stimulation Versus Conventional Stimulation in Parkinson's Disease: A Blinded Randomized Feasibility Trial. *Nat. Med.* **2024**, *30*, 3345–3356.
- (10) Rajamani, N.; Friedrich, H.; Butenko, K.; Dembek, T.; Lange, F.; Navrátil, P.; Zvarova, P.; Hollunder, B.; de Bie, R. M. A.; Odekerken, V. J. J.; Volkmann, J.; Xu, X.; Ling, Z.; Yao, C.; Ritter, P.; Neumann, W. J.; Skandalakis, G. P.; Komaitis, S.; Kalyvas, A.; Koutsarnakis, C.; Stranjalis, G.; Barbe, M.; Milanese, V.; Fox, M. D.; Kühn, A. A.; Middlebrooks, E.; Li, N.; Reich, M.; Neudorfer, C.; Horn, A. Deep Brain Stimulation of Symptom-Specific Networks in Parkinson's Disease. *Nat. Commun.* **2024**, *15*, 4662.
- (11) Vitek, J. L.; Jain, R.; Chen, L.; Tröster, A. I.; Schrock, L. E.; House, P. A.; Giroux, M. L.; Hebb, A. O.; Farris, S. M.; Whiting, D. M.; Leichliter, T. A.; Ostrem, J. L.; San Luciano, M.; Galifianakis, N.; Verhagen Metman, L.; Sani, S.; Karl, J. A.; Siddiqui, M. S.; Tatter, S. B.; ul Haq, I.; Machado, A. G.; Gostkowski, M.; Tagliati, M.; Mamelak, A. N.; Okun, M. S.; Foote, K. D.; Moguel-Cobos, G.; Ponce, F. A.; Pahwa, R.; Nazzaro, J. M.; Buetefisch, C. M.; Gross, R. E.; Luca, C. C.; Jagid, J. R.; Revuelta, G. J.; Takacs, I.; Pourfar, M. H.; Mogilner, A. Y.; Duker, A. P.; Mandybur, G. T.; Rosenow, J. M.; Cooper, S. E.; Park, M. C.; Khandhar, S. M.; Sedrak, M.; Phibbs, F. T.; Pilitsis, J. G.; Uitti, R. J.; Starr, P. A. Subthalamic nucleus deep brain stimulation with a multiple independent constant current-controlled device in Parkinson's disease (INTREPID): a multicentre, double-blind, randomised, sham-controlled study. *Lancet Neurol.* 2020, 19, 491–501.
- (12) Lange, M.; Mauerer, J.; Schlaier, J.; Janzen, A.; Zeman, F.; Bogdahn, U.; Brawanski, A.; Hochreiter, A. Underutilization of Deep

- Brain Stimulation for Parkinson's Disease? A Survey on Possible Clinical Reasons. *Acta Neurochir.* **2017**, *159*, 771–778.
- (13) Chen, S.; Weitemier, A. Z.; Zeng, X.; He, L.; Wang, X.; Tao, Y.; Huang, A. J. Y.; Hashimotodani, Y.; Kano, M.; Iwasaki, H.; Parajuli, L. K.; Okabe, S.; Teh, D. B. L.; All, A. H.; Tsutsui-Kimura, I.; Tanaka, K. F.; Liu, X.; McHugh, T. J. Near-Infrared Deep Brain Stimulation Via Upconversion Nanoparticle-Mediated Optogenetics. *Science* **2018**, 359, 679–684.
- (14) Wu, X.; Jiang, Y.; Rommelfanger, N. J.; Yang, F.; Zhou, Q.; Yin, R.; Liu, J.; Cai, S.; Ren, W.; Shin, A.; Ong, K. S.; Pu, K.; Hong, G. Tether-Free Photothermal Deep-Brain Stimulation in Freely Behaving Mice Via Wide-Field Illumination in the near-Infrared-Ii Window. *Nat. Biomed. Eng.* **2022**, *6*, 754–770.
- (15) Xian, Q.; Qiu, Z.; Murugappan, S.; Kala, S.; Wong, K. F.; Li, D.; Li, G.; Jiang, Y.; Wu, Y.; Su, M.; Hou, X.; Zhu, J.; Guo, J.; Qiu, W.; Sun, L. Modulation of Deep Neural Circuits with Sonogenetics. *Proc. Natl. Acad. Sci. U. S. A.* **2023**, *120*, No. e2220575120.
- (16) Keiser, M. S.; Ranum, P. T.; Yrigollen, C. M.; Carrell, E. M.; Smith, G. R.; Muehlmatt, A. L.; Chen, Y. H.; Stein, J. M.; Wolf, R. L.; Radaelli, E.; Lucas, T. J.; Gonzalez-Alegre, P.; Davidson, B. L. Toxicity after Aav Delivery of Rnai Expression Constructs into Nonhuman Primate Brain. *Nat. Med.* 2021, 27, 1982–1989.
- (17) Wu, J.; Cui, X.; Bao, L.; Liu, G.; Wang, X.; Chen, C. A Nanoparticle-Based Wireless Deep Brain Stimulation System That Reverses Parkinson's Disease. *Sci. Adv.* **2025**, *11*, No. eado4927.
- (18) Zhang, Z.; Luo, Y.; Ma, Y.; Zhou, Y.; Zhu, D.; Shen, W.; Liu, J. Photocatalytic Manipulation of Ca²⁺ Signaling for Regulating Cellular and Animal Behaviors via MOF-Enabled H₂O₂ Generation. *Sci. Adv.* **2024**, *10*, No. eadl0263.
- (19) Limousin, P.; Foltynie, T. Long-Term Outcomes of Deep Brain Stimulation in Parkinson Disease. *Nat. Rev. Neurol.* **2019**, *15*, 234–242
- (20) Dias, V.; Junn, E.; Mouradian, M. M. The Role of Oxidative Stress in Parkinson's Disease. *J. Parkinsons Dis.* **2013**, *3*, 461–491.
- (21) Jiang, W.; Li, Q.; Zhang, R.; Li, J.; Lin, Q.; Li, J.; Zhou, X.; Yan, X.; Fan, K. Chiral Metal-Organic Frameworks Incorporating Nanozymes as Neuroinflammation Inhibitors for Managing Parkinson's Disease. *Nat. Commun.* **2023**, *14*, 8137.
- (22) Liu, Z.; Xiang, S.; Chen, B.; Li, J.; Zhu, D.; Xu, H.; Hu, S. Parkinson Disease-Targeted Nanocapsules for Synergistic Treatment: Combining Dopamine Replacement and Neuroinflammation Mitigation. *Adv. Sci.* **2024**, *11*, No. 2404717.
- (23) Li, Q.; Wu, T.; Akakuru, O. U.; Song, N.; Liu, W.; Jiang, W.; Fan, K. A Dual Synergetic Nanoreactor for Managing Parkinson's Disease by Regulating Inflammation and Mitigating Oxidative Damage. *Adv. Funct. Mater.* **2023**, *33*, No. 2214826.
- (24) Wu, D.; Zhou, J.; Zheng, Y.; Zheng, Y.; Zhang, Q.; Zhou, Z.; Chen, X.; Chen, Q.; Ruan, Y.; Wang, Y.; Chen, Z. Pathogenesis-Adaptive Polydopamine Nanosystem for Sequential Therapy of Ischemic Stroke. *Nat. Commun.* **2023**, *14*, 7147.
- (25) Zheng, Y.; Chen, X.; Zhang, Q.; Yang, L.; Chen, Q.; Chen, Z.; Wang, Y.; Wu, D. Evaluation of Reactive Oxygen Species Scavenging of Polydopamine with Different Nanostructures. *Adv. Healthcare Mater.* **2024**, *13*, No. 2302640.
- (26) Prasad, P.; Gordijo, C. R.; Abbasi, A. Z.; Maeda, A.; Ip, A.; Rauth, A. M.; DaCosta, R. S.; Wu, X. Y. Multifunctional Albumin-Mno₂ Nanoparticles Modulate Solid Tumor Microenvironment by Attenuating Hypoxia, Acidosis, Vascular Endothelial Growth Factor and Enhance Radiation Response. *ACS Nano* **2014**, *8*, 3202–3212.
- (27) Shah, H. U.; Wang, F.; Javed, M. S.; Saleem, R.; Nazir, M. S.; Zhan, J.; Khan, Z. U. H.; Farooq, M. U.; Ali, S. Synthesis, Characterization and Electrochemical Properties of A-Mno₂ Nanowires as Electrode Material for Supercapacitors. *Int. J. Electrochem. Sci.* **2018**, *13*, 6426–6435.
- (28) Li, W.; Zeng, R.; Sun, Z.; Tian, D.; Dou, S. Uncoupled Surface Spin Induced Exchange Bias in A-Mno₂ Nanowires. *Sci. Rep.* **2014**, *4*, 6641
- (29) Yim, W.; Borum, R. M.; Zhou, J.; Mantri, Y.; Wu, Z.; Zhou, J.; Jin, Z.; Creyer, M.; Jokerst, J. V. Ultrasmall Gold Nanorod-

- Polydopamine Hybrids for Enhanced Photoacoustic Imaging and Photothermal Therapy in Second near-Infrared Window. *Nanotheranostics* **2022**, *6*, 79.
- (30) Deng, X.; Liang, S.; Cai, X.; Huang, S.; Cheng, Z.; Shi, Y.; Pang, M.; Ma, P. a.; Lin, J. Yolk—Shell Structured Au Nanostar@Metal—Organic Framework for Synergistic Chemo-Photothermal Therapy in the Second near-Infrared Window. *Nano Lett.* **2019**, *19*, 6772—6780.
- (31) Halliwell, B. Understanding Mechanisms of Antioxidant Action in Health and Disease. *Nat. Rev. Mol. Cell Biol.* **2024**, *25*, 13–33.
- (32) Huang, X.; Yin, Y.; Tang, Y.; Bai, X.; Zhang, Z.; Xu, J.; Liu, J.; Shen, J. Smart Microgel Catalyst with Modulatory Glutathione Peroxidase Activity. *Soft Matter* **2009**, *5*, 1905–1911.
- (33) Lin, J.-H.; Yu, C.-J.; Yang, Y.-C.; Tseng, W.-L. Formation of Fluorescent Polydopamine Dots from Hydroxyl Radical-Induced Degradation of Polydopamine Nanoparticles. *Phys. Chem. Chem. Phys.* **2015**, *17*, 15124–15130.
- (34) Stykel, M. G.; Ryan, S. D. Nitrosative Stress in Parkinson's Disease. *npj Parkinson's Dis.* **2022**, *8*, 104.
- (35) Lin, L. S.; Song, J.; Song, L.; Ke, K.; Liu, Y.; Zhou, Z.; Shen, Z.; Li, J.; Yang, Z.; Tang, W.; Niu, G.; Yang, H.; Chen, X. Simultaneous Fenton-Like Ion Delivery and Glutathione Depletion by Mno₂-Based Nanoagent to Enhance Chemodynamic Therapy. *Angew. Chem., Int. Ed.* **2018**, *130*, 4996–5000.
- (36) Hernandez-Baltazar, D.; Zavala-Flores, L.; Villanueva-Olivo, A. The 6-Hydroxydopamine Model and Parkinsonian Pathophysiology: Novel Findings in an Older Model. *Neurologia (English Edition)* **2017**, 32, 533–539.
- (37) Bao, X.; Zhao, J.; Sun, J.; Hu, M.; Yang, X. Polydopamine Nanoparticles as Efficient Scavengers for Reactive Oxygen Species in Periodontal Disease. *ACS Nano* **2018**, *12*, 8882–8892.
- (38) Zhou, F.; He, Y.; Zhang, M.; Gong, X.; Liu, X.; Tu, R.; Yang, B. Polydopamine (Pda)-Coated Diselenide-Bridged Mesoporous Silica-Based Nanoplatform for Neuroprotection by Reducing Oxidative Stress and Targeting Neuroinflammation in Intracerebral Hemorrhage. *J. Nanobiotechnol.* **2024**, *22*, 731.
- (39) Tian, R.; Ma, H.; Ye, W.; Li, Y.; Wang, S.; Zhang, Z.; Liu, S.; Zang, M.; Hou, J.; Xu, J.; Luo, Q.; Sun, H.; Bai, F.; Yang, Y.; Liu, J. Se-Containing Mof Coated Dual-Fe-Atom Nanozymes with Multi-Enzyme Cascade Activities Protect against Cerebral Ischemic Reperfusion Injury. *Adv. Funct. Mater.* **2022**, *32*, No. 2204025.
- (40) He, X.; Yuan, W.; Yang, C.-Q.; Zhu, L.; Liu, F.; Feng, J.; Xue, Y.-X. Ghrelin Alleviates 6-Hydroxydopamine-Induced Neurotoxicity in Sh-Sy5y Cells. *Neural Regen. Res.* **2022**, *17*, 170–177.
- (41) Li, Y.; Liu, Z.; Wang, D.; Gao, H.; Zhu, Z.; Wang, Y.; Luo, Q.; Jiang, S.; Zhang, J.; Yang, X. Ucf-101 Protects in Vivo and in Vitro Models of Pd against 6-Hydroxydopamine Toxicity by Alleviating Endoplasmic Reticulum Stress Via the Wnt/B-Catenin Pathway. *J. Clin. Neurosci.* 2020, 71, 217–225.
- (42) Gan, X.; Ren, J.; Huang, T.; Wu, K.; Li, S.; Duan, Y.; Wang, Z.; Si, W.; Wei, J. Pathological A-Synuclein Accumulation, Csf Metabolites Changes and Brain Microstructures in Cynomolgus Monkeys Treated with 6-Hydroxydopamine. *Neurotoxicology* **2023**, *94*, 172–181.
- (43) Hijaz, B. A.; Volpicelli-Daley, L. A. Initiation and Propagation of A-Synuclein Aggregation in the Nervous System. *Mol. Neuro-degener.* **2020**, *15*, 19.
- (44) Zhu, D.; Feng, L.; Feliu, N.; Guse, A. H.; Parak, W. J. Stimulation of Local Cytosolic Calcium Release by Photothermal Heating for Studying Intra- and Intercellular Calcium Waves. *Adv. Mater.* **2021**, 33, No. 2008261.
- (45) Pinto, B. I.; Bassetto, C. A., Jr; Bezanilla, F. Optocapacitance: Physical Basis and Its Application. *Biophys. Rev.* **2022**, *14*, 569–577.
- (46) Itoh, H.; Oyama, K.; Suzuki, M.; Ishiwata, S. I. Microscopic Heat Pulse-Induced Calcium Dynamics in Single Wi-38 Fibroblasts. *Biophysics* **2014**, *10*, 109–119.
- (47) Wang, Y.; Garg, R.; Hartung, J. E.; Goad, A.; Patel, D. A.; Vitale, F.; Gold, M. S.; Gogotsi, Y.; Cohen-Karni, T. Ti₃c₂t_x Mxene Flakes for Optical Control of Neuronal Electrical Activity. *ACS Nano* **2021**, *15*, 14662–14671.

- (48) Jiang, Y.; Li, X.; Liu, B.; Yi, J.; Fang, Y.; Shi, F.; Gao, X.; Sudzilovsky, E.; Parameswaran, R.; Koehler, K.; Nair, V.; Yue, J.; Guo, K.; Fang, Y.; Tsai, H. M.; Freyermuth, G.; Wong, R. C. S.; Kao, C. M.; Chen, C. T.; Nicholls, A. W.; Wu, X.; Shepherd, G. M. G.; Tian, B. Rational Design of Silicon Structures for Optically Controlled Multiscale Biointerfaces. *Nat. Biomed. Eng.* **2018**, *2*, 508–521.
- (49) Daubner, S. C.; Le, T.; Wang, S. Tyrosine Hydroxylase and Regulation of Dopamine Synthesis. *Arch. Biochem. Biophys.* **2011**, *508*, 1–12.
- (50) Gueorguiev, V. D.; Zeman, R. J.; Hiremagalur, B.; Menezes, A.; Sabban, E. L. Differing Temporal Roles of Ca²⁺ and Camp in Nicotine-Elicited Elevation of Tyrosine Hydroxylase Mrna. *Am. J. Physiol. Cell Physiol.* **1999**, 276, C54–C65.
- (51) Hiremagalur, B.; Nankova, B.; Nitahara, J.; Zeman, R.; Sabban, E. Nicotine Increases Expression of Tyrosine Hydroxylase Gene. Involvement of Protein Kinase a-Mediated Pathway. *J. Biol. Chem.* 1993, 268, 23704–23711.
- (52) Salvatore, M. F.; Waymire, J. C.; Haycock, J. W. Depolarization-Stimulated Catecholamine Biosynthesis: Involvement of Protein Kinases and Tyrosine Hydroxylase Phosphorylation Sites in Situ. *J. Neurochem.* **2001**, *79*, 349–360.
- (53) Kim, K.-S.; Park, D. H.; Wessel, T. C.; Song, B.; Wagner, J. A.; Joh, T. H. A Dual Role for the Camp-Dependent Protein Kinase in Tyrosine Hydroxylase Gene Expression. *Proc. Natl. Acad. Sci. U. S. A.* 1993, *90*, 3471–3475.
- (54) Gubernator, N. G.; Zhang, H.; Staal, R. G. W.; Mosharov, E. V.; Pereira, D. B.; Yue, M.; Balsanek, V.; Vadola, P. A.; Mukherjee, B.; Edwards, R. H.; Sulzer, D.; Sames, D. Fluorescent False Neurotransmitters Visualize Dopamine Release from Individual Presynaptic Terminals. *Science* **2009**, 324, 1441–1444.
- (55) Patel, J. C.; Witkovsky, P.; Avshalumov, M. V.; Rice, M. E. Mobilization of Calcium from Intracellular Stores Facilitates Somatodendritic Dopamine Release. *J. Neurosci.* **2009**, *29*, 6568–6579.
- (56) Zhou, Q.; Shao, S.; Wang, J.; Xu, C.; Xiang, J.; Piao, Y.; Zhou, Z.; Yu, Q.; Tang, J.; Liu, X.; Gan, Z.; Mo, R.; Gu, Z.; Shen, Y. Enzyme-Activatable Polymer-Drug Conjugate Augments Tumour Penetration and Treatment Efficacy. *Nat. Nanotechnol.* **2019**, *14*, 799–809.
- (57) Liu, W.; Gao, T.; Li, N.; Shao, S.; Liu, B. Vesicle Fusion and Release in Neurons under Dynamic Mechanical Equilibrium. *Iscience* **2024**, *27*, No. 109793.
- (58) Huang, J.; Ye, Z.; Hu, X.; Lu, L.; Luo, Z. Electrical Stimulation Induces Calcium-Dependent Release of Ngf from Cultured Schwann Cells. *Glia* **2010**, *58*, 622–631.
- (59) Chen, J.; Liu, Y.; Chen, F.; Guo, M.; Zhou, J.; Fu, P.; Zhang, X.; Wang, X.; Wang, H.; Hua, W.; Chen, J.; Hu, J.; Mao, Y.; Jin, D.; Bu, W.; et al. Non-Faradaic Optoelectrodes for Safe Electrical Neuromodulation. *Nat. Commun.* **2024**, *15*, 405.
- (60) Gao, Y.; Guo, Y.; Yang, Y.; Tang, Y.; Wang, B.; Yan, Q.; Chen, X.; Cai, J.; Fang, L.; Xiong, Z.; Gao, F.; Wu, C.; Wang, J.; Tang, J.; Shi, L.; Li, D. Magnetically Manipulated Optoelectronic Hybrid Microrobots for Optically Targeted Non-Genetic Neuromodulation. *Adv. Mater.* **2024**, *36*, No. 2305632.
- (61) Haesemeyer, M.; Robson, D. N.; Li, J. M.; Schier, A. F.; Engert, F. A Brain-Wide Circuit Model of Heat-Evoked Swimming Behavior in Larval Zebrafish. *Neuron* **2018**, *98*, 817–831e816.
- (62) Jackson-Lewis, V.; Przedborski, S. Protocol for the Mptp Mouse Model of Parkinson's Disease. *Nat. Protoc.* **2007**, *2*, 141–151.
- (63) McKinnon, C.; Gros, P.; Lee, D. J.; Hamani, C.; Lozano, A. M.; Kalia, L. V.; Kalia, S. K. Deep Brain Stimulation: Potential for Neuroprotection. *Ann. Clin. Transl. Neurol.* **2019**, *6*, 174–185.
- (64) Zhang, C.; Jing, X.; Guo, L.; Cui, C.; Hou, X.; Zuo, T.; Liu, J.; Shi, J.; Liu, X.; Zuo, X.; Li, J.; Chang, C.; Fan, C.; Wang, L. Remote Photothermal Control of DNA Origami Assembly in Cellular Environments. *Nano Lett.* **2021**, *21*, 5834–5841.
- (65) Zhang, C.; Yuan, Y.; Wu, K.; Wang, Y.; Zhu, S.; Shi, J.; Wang, L.; Li, Q.; Zuo, X.; Fan, C.; Chang, C.; Li, J. Driving DNA Origami Assembly with a Terahertz Wave. *Nano Lett.* **2021**, *22*, 468–475.

- (66) Li, L.; He, S.; Liao, B.; Wang, M.; Lin, H.; Hu, B.; Lan, X.; Shu, Z.; Zhang, C.; Yu, M.; Zou, Z. Orally Administrated Hydrogel Harnessing Intratumoral Microbiome and Microbiota-Related Immune Responses for Potentiated Colorectal Cancer Treatment. *Research* 2024, 7, No. 0364.
- (67) Chu, X.; Jiang, X.; Liu, Y.; Zhai, S.; Jiang, Y.; Chen, Y.; Wu, J.; Wang, Y.; Wu, Y.; Tao, X.; He, X.; Bu, W. Nitric Oxide Modulating Calcium Store for Ca²⁺-Initiated Cancer Therapy. *Adv. Funct. Mater.* **2021**, *31*, No. 2008507.
- (68) Hu, J.; Yuan, L.; Zhang, Y.; Kuang, J.; Song, W.; Lou, X.; Xia, F.; Yoon, J. Photo-Controlled Calcium Overload from Endogenous Sources for Tumor Therapy. *Angew. Chem., Int. Ed.* **2024**, *63*, No. e202317578.
- (69) Rosenfeld, D.; Senko, A. W.; Moon, J.; Yick, I.; Varnavides, G.; Gregureć, D.; Koehler, F.; Chiang, P. H.; Christiansen, M. G.; Maeng, L. Y.; Widge, A. S.; Anikeeva, P. Transgene-Free Remote Magnetothermal Regulation of Adrenal Hormones. *Sci. Adv.* **2020**, *6*, No. eaaz3734.
- (70) Xiong, H.; Alberto, K. A.; Youn, J.; Taura, J.; Morstein, J.; Li, X.; Wang, Y.; Trauner, D.; Slesinger, P. A.; Nielsen, S. O.; Qin, Z. Optical Control of Neuronal Activities with Photoswitchable Nanovesicles. *Nano Res.* **2022**, *16*, 1033–1041.
- (71) Xiong, H.; Li, X.; Kang, P.; Perish, J.; Neuhaus, F.; Ploski, J. E.; Kroener, S.; Ogunyankin, M. O.; Shin, J. E.; Zasadzinski, J. A.; Wang, H.; Slesinger, P. A.; Zumbuehl, A.; Qin, Z. Near-Infrared Light Triggered-Release in Deep Brain Regions Using Ultra-Photosensitive Nanovesicles. *Angew. Chem., Int. Ed.* **2020**, *59*, 8608–8615.
- (72) Chen, G.; Yu, F.; Shi, L.; Marar, C.; Du, Z.; Jia, D.; Cheng, J.; Yang, C. High-Precision Photoacoustic Neural Modulation Uses a Non-Thermal Mechanism. *Adv. Sci.* **2024**, *11*, No. 2403205.
- (73) Beckham, J. L.; van Venrooy, A. R.; Kim, S.; Li, G.; Li, B.; Duret, G.; Arnold, D.; Zhao, X.; Li, J. T.; Santos, A. L.; Chaudhry, G.; Liu, D.; Robinson, J. T.; Tour, J. M. Molecular Machines Stimulate Intercellular Calcium Waves and Cause Muscle Contraction. *Nat. Nanotechnol.* **2023**, *18*, 1051–1059.
- (74) Chen, X.; Zhang, X.; Kubo, H.; Harris, D. M.; Mills, G. D.; Moyer, J.; Berretta, R.; Potts, S. T.; Marsh, J. D.; Houser, S. R. Ca²⁺ Influx-Induced Sarcoplasmic Reticulum Ca²⁺ Overload Causes Mitochondrial-Dependent Apoptosis in Ventricular Myocytes. *Circ. Res.* **2005**, *97*, 1009–1017.
- (75) Gielecińska, A.; Kciuk, M.; Kontek, R. The Impact of Calcium Overload on Cellular Processes: Exploring Calcicoptosis and Its Therapeutic Potential in Cancer. *Int. J. Mol. Sci.* **2024**, 25, 13727.
- (76) Zhou, Y.; Zhang, Z.; Zhou, C.; Ma, Y.; Huang, H.; Liu, J.; Zhu, D. Nanotechnology-Fortified Manipulation of Cell Ca²⁺ Signaling. *Small Sci.* **2024**, *4*, No. 2400169.
- (77) Emami, N. K.; Jung, U.; Voy, B.; Dridi, S. Radical Response: Effects of Heat Stress-Induced Oxidative Stress on Lipid Metabolism in the Avian Liver. *Antioxidants* **2021**, *10*, 35.
- (78) Venkataraman, S.; Wagner, B. A.; Jiang, X.; Wang, H. P.; Schafer, F. Q.; Ritchie, J. M.; Patrick, B. C.; Oberley, L. W.; Buettner, G. R. Overexpression of Manganese Superoxide Dismutase Promotes the Survival of Prostate Cancer Cells Exposed to Hyperthermia. *Free Radic. Res.* **2004**, *38*, 1119–1132.
- (79) White, M. G.; Saleh, O.; Nonner, D.; Barrett, E. F.; Moraes, C. T.; Barrett, J. N. Mitochondrial Dysfunction Induced by Heat Stress in Cultured Rat Cns Neurons. *J. Neurophysiol.* **2012**, *108*, 2203–2214.
- (80) Zeng, W.; Li, Z.; Huang, Q.; Ding, C.; Yang, L.; Wang, W.; Shi, Z.; Yang, Y.; Chen, H.; Mei, L.; Zeng, X. Multifunctional Mesoporous Polydopamine-Based Systematic Delivery of Sting Agonist for Enhanced Synergistic Photothermal-Immunotherapy. *Adv. Funct. Mater.* **2024**, 34, No. 2307241.
- (81) Xu, L. Q.; Yang, W. J.; Neoh, K.-G.; Kang, E.-T.; Fu, G. D. Dopamine-Induced Reduction and Functionalization of Graphene Oxide Nanosheets. *Macromolecules* **2010**, *43*, 8336–8339.
- (82) Ai, Y.; Zhang, Z.; Fei, Y.; Ye, R.; Law, A. S.-Y.; Mao, Z.-W.; Liu, J.; Li, Y.; Yam, V. W.-W. Rational Design of Platinum (Ii) Complexes with Orthogonally Oriented Triazolyl Ligand with Emission Enhance-

ment Characteristics for Cancer Chemotherapy in Vivo. Sci. China Chem. 2023, 66, 2878–2884.

- (83) Felice, D. L.; Sun, J.; Liu, R. H. A Modified Methylene Blue Assay for Accurate Cell Counting. *J. Funct. Foods* **2009**, *1*, 109–118.
- (84) Liu, C.; Kaeser, P. S. Mechanisms and Regulation of Dopamine Release. *Curr. Opin. Neurobiol.* **2019**, *57*, 46–53.
- (85) Westerfield, M.A Guide for the Laboratory Use of Zebrafish Danio (Brachydanio) Rerio. In *The Zebrafish Book*, 5th ed., Zebrafish International Resource Center: OR, 2007, Vol. 5.
- (86) Li, J.; Zhang, B.-b.; Ren, Y.-g.; Gu, S.-y.; Xiang, Y.-h.; Huang, C.; Du, J.-l. Intron Targeting-Mediated and Endogenous Gene Integrity-Maintaining Knockin in Zebrafish Using the Crispr/Cas9 System. *Cell Res.* **2015**, *25*, 634–637.



CAS BIOFINDER DISCOVERY PLATFORM™

STOP DIGGING THROUGH DATA —START MAKING DISCOVERIES

CAS BioFinder helps you find the right biological insights in seconds

Start your search

